

https://doi.org/10.1093/plcell/koae145 Advance access publication 9 May 2024

Research Article

A prion-like domain is required for phase separation and chloroplast RNA processing during cold acclimation in Arabidopsis

Julia Legen, ¹ 🐌 Benjamin Lenzen, ¹ 🐌 Nitin Kachariya, ^{2,3}📵 Stephanie Feltgen, ¹📵 Yang Gao, ⁴📵 Simon Mergenthal, ⁵📵 Willi Weber, 6 Enrico Klotzsch, 6 Reimo Zoschke, 6 Michael Sattler, 6 and Christian Schmitz-Linneweber 1.* 10 and Christian Schmitz-Linneweber 1.* 10 Annual Schmitz-

The author responsible for distribution of materials integral to the findings presented in this article in accordance with the policy described in the Instructions for Authors (https://academic.oup.com/plcell/pages/General-Instructions) is: Christian Schmitz-Linneweber.

Abstract

Arabidopsis (Arabidopsis thaliana) plants can produce photosynthetic tissue with active chloroplasts at temperatures as low as 4°C, and this process depends on the presence of the nuclear-encoded, chloroplast-localized RNA-binding protein CP29A. In this study, we demonstrate that CP29A undergoes phase separation in vitro and in vivo in a temperature-dependent manner, which is mediated by a prion-like domain (PLD) located between the two RNA recognition motif domains of CP29A. The resulting droplets display liquid-like properties and are found near chloroplast nucleoids. The PLD is required to support chloroplast RNA splicing and translation in coldtreated tissue. Together, our findings suggest that plant chloroplast gene expression is compartmentalized by inducible condensation of CP29A at low temperatures, a mechanism that could play a crucial role in plant cold resistance.

Introduction

Phase separation (PS) is a phenomenon that can lead to the formation of membrane-less compartments within cells (Shin and Brangwynne 2017). These compartments are a dynamic alternative to organelles, as they lack a physical, membranous boundary and can be modulated by changes in protein concentrations, metabolites, salt and temperature (Alberti and Hyman 2021). Compartments induced by PS are important for efficiently organizing cellular processes by concentrating specific factors at the appropriate place and time. Unlike irreversible protein aggregation, these compartments are dynamically formed and dissolved and often have a viscoelastic-dynamic, fluid nature, which makes them flexible and adaptable (Shin and Brangwynne 2017), although more granular structures have been shown to serve biological functions as well (Boke et al. 2016; Woodruff et al. 2017; Bose et al. 2022). PS is crucial for rapid responses to changing environments, and can be induced by shifts in temperature and cellular homeostasis (Nott et al. 2015; Dignon et al. 2019). Intrinsically disordered protein domains (IDRs) are often at the heart of PS phenomena, driving the formation of cellular membrane-less compartments through multivalent interactions (Kato et al. 2012; Forman-Kay and Mittag 2013). RNA can act as a seed and essential component for phase-separated compartments, with RNA-binding proteins being over-represented among factors described to phase-separate (Roden and Gladfelter 2021). PS and the resulting RNA granules play a crucial role in a number of processes involving RNA-binding proteins, including ribosome maturation, RNA splicing, ribonucleoprotein biogenesis, and RNA degradation.

In plants, PS phenomena are just beginning to be characterized (Emenecker et al. 2020; Gutierrez-Beltran et al. 2023; Kang and Xu 2023), but it is already clear that condensates contribute to stress resilience and signaling (Kearly et al. 2022; Field et al. 2023; Solis-Miranda et al. 2023). Almost all of the PS events described in land plants occur in the cytosol or the cytoplasm (Fang et al. 2019; Jung et al. 2020; Zavaliev et al. 2020; Huang et al. 2021b; Kim et al. 2021; Xie et al. 2021; Zhang et al. 2022; Hoffmann et al. 2023; Ruiz-Solaní et al. 2023; Shang et al. 2023; Tan et al. 2023; Wang et al. 2023), but there is one notable exception: In Arabidopsis chloroplasts, an ankyrin protein has been shown to undergo PS to facilitate sorting and transport of proteins into the thylakoids (Ouyang et al. 2020). PS also plays a role in chloroplasts of green algae, where the chloroplast pyrenoid, a structure required for carbon concentration around Rubisco, has been shown to assemble via condensation (Rosenzweig et al. 2017). There are also reports of RNA granules in the chloroplast of a green alga, but whether they are based on PS phenomena is unclear (Uniacke and Zerges 2009, 2008). Similarly, heat inducible stress granules were observed in Arabidopsis chloroplasts, but the influence of PS is unclear (Chodasiewicz et al. 2020).

The chloroplast RNA-binding protein CP29A is a member of the cpRNP protein family, which has 11 representatives in

¹Molecular Genetics, Humboldt Universität zu Berlin, Philippstrasse 13, Berlin 10115, Germany

 $^{^2}$ Helmholtz Munich, Institute of Structural Biology, Ingolstädter Landstrasse 1, Munich 85764, Germany

³Department of Bioscience, Bayarian NMR Center, TUM School of Natural Sciences, Technical University of Munich, Lichtenbergstrasse 4, Garching 85747, Germany

⁴Max Planck Institute of Molecular Plant Physiology, Am Mühlenberg 1, Potsdam-Golm 14476, Germany

⁵Institute for Biology, Experimental Biophysics/Mechanobiology, Humboldt-Universität zu Berlin, Invalidenstrasse 42, Berlin 10115, Germany

^{*}Author for correspondence: christian.schmitz-linneweber@rz.hu-berlin.de

[†]These authors contributed equally to this work.

IN A NUTSHELL

Background: Many mutants of chloroplast RNA-binding proteins exhibit cold-specific phenotypes at temperatures well above freezing. Such cold acclimation is common for temperate zone plants like Arabidopsis throughout much of the year. An example of a chloroplast RNA-binding protein with cold-protective functions is the twin-RNA-recognition motif protein CP29A. CP29A causes bleaching of the youngest tissue at the center of the leaf rosette after extended exposure to low temperatures. The mechanism by which CP29A ensures proper chloroplast development in the cold remains unclear.

Question: How do chloroplast RNA metabolism in general, and the chloroplast RNA-binding protein CP29A specifically, contribute to the cold resistance of plants?

Findings: CP29A contains a prion-like domain (PLD) that confers autonomous and cold-dependent phase-separating ability both in vitro and in vivo. Structural analyses suggest that charged interactions of the PLD contribute to the formation of a condensed phase. These condensates can take up chloroplast RNAs and form in close proximity to the chloroplast nucleoid in vivo, potentially linking transcription and post-transcriptional processes. Such a compartmentalization of chloroplast gene expression in land plants was previously unknown. Null mutants of CP29A show reduced RNA splicing of chloroplast introns not only in bleached tissue but also early after cold challenges, before the paleness of the young tissue becomes visible. Using Ribo-Seq, we also observe a cold-induced global reduction of chloroplast translation in CP29A mutants, which may be a secondary consequence of the splicing defects. In summary, our data indicate that CP29A confers cold-acclimation ability to plants by supporting efficient, localized chloroplast RNA processing.

Next steps: Most target RNAs identified in previous RNA co-immunoprecipitation experiments do not contain introns, prompting the question of whether CP29A itself is a splicing factor or rather a scaffold protein in phase separation. To address this, the protein and RNA composition of CP29A droplets needs to be elucidated, and the molecular function of CP29A for intron-containing and nonintron-containing RNAs needs to be investigated, for example, in RNA structure remodeling. A more general question emerging from this work is whether subcompartmentation by phase separation is more prevalent in chloroplasts than previously anticipated.

Arabidopsis, all localizing to chloroplasts (Ruwe et al. 2011). Unlike the other 10 family members, CP29A's two RNA recognition motifs (RRMs) are spaced by a linker of 84 amino acids. CP29A responds to different external and internal stimuli, accumulating to higher levels in the cold and being repressed by other stressors and abscisic acid (Raab et al. 2006; Kupsch et al. 2012). CP29A associates with a large number of chloroplast transcripts (Kupsch et al. 2012). A homologue of CP29A in Nicotiana tabacum is required for stabilizing chloroplast RNAs in vitro (Nakamura et al. 2001). Null mutants of CP29A exhibit a pale center of the leaf rosette after long-term exposure to low temperatures, with defects in chloroplast RNA processing and accumulation (Kupsch et al. 2012). When grown at regular growth temperatures, CP29A-deficient plants do not show RNA defects or macroscopic changes relative to wild-type (wt) plants, indicating that CP29A has evolved to support cold acclimation in Arabidopsis (Kupsch et al. 2012). The temperature range in which CP29A is relevant does not fall within the realm of stress, but rather within a range that plants such as Arabidopsis are constantly exposed to in temperate zones, specifically from 4 to 12°C. Therefore, CP29A is a factor that is crucial for the daily acclimatization to low temperatures, which are to be expected throughout the year in temperate regions. The molecular mechanisms by which CP29A achieves this acclimatization of plastid RNA metabolism and prevents bleaching remains unclear, nor was it determined whether the effects on RNA maturation and accumulation observed in pale tissue were of primary origin or are pleiotropic effects of the nonphotosynthetic tissue. We report here that CP29A is capable of forming droplets in vitro and in vivo via its prion-like domain (PLD) and that the PLD is required for chloroplast splicing, translation, and cold resistance.

Results

The organellar RNA-binding protein CP29A has a PLD, which is required for PS in vitro

The protein CP29A contains two RRMs that are separated by a linker domain consisting of 84 amino acids. This linker has a repetitive, low complexity sequence with charged and polar residues, and is intrinsically disordered with a prion-like amino acid composition according to in silico predictions using the PLAAC and the SPOTD tool (Fig. 1A; Lancaster et al. 2014; Hanson et al. 2019). To determine whether CP29A can undergo PS, we used recombinant, purified, untagged CP29A and monitored its behavior at different temperatures. We found that the CP29A solution becomes turbid at low—but still physiological—temperatures (4°C) within a few minutes in the presence of crowding reagent, but returns to full translucence when brought back to room temperature (25°C; Fig. 1B, Supplementary Video S1). This indicates that condensate formation is reversible at least for freshly formed droplets. Without addition of PEG, the protein remains in solution at room temperature. However, after cooling on ice for 5 min, microscopic inspection reveals numerous droplets in the absence of PEG, demonstrating that CP29A can phase-separate at low temperatures in the absence of crowding reagents (Fig. 1C). By contrast, the protein precipitates irreversibly when heated to 37°C (Fig. 1B). Next, we analyzed whether full-length CP29A, the PLD alone or a PLD-deletion protein can form liquid droplets. For the PLD deletion, we removed 60 amino acids comprising the glycine-rich region, but still leaving a linker between the RRMs of 16 amino acids (Supplementary Fig. S1A). With the exception of CP29A, all other cpRNP family members have short linkers; for example, CP28A has a linker of 18 residues and CP33B has 26 residues (Supplementary Fig. S1A). We, therefore, speculate that within this protein family, the two RRM domains are functional

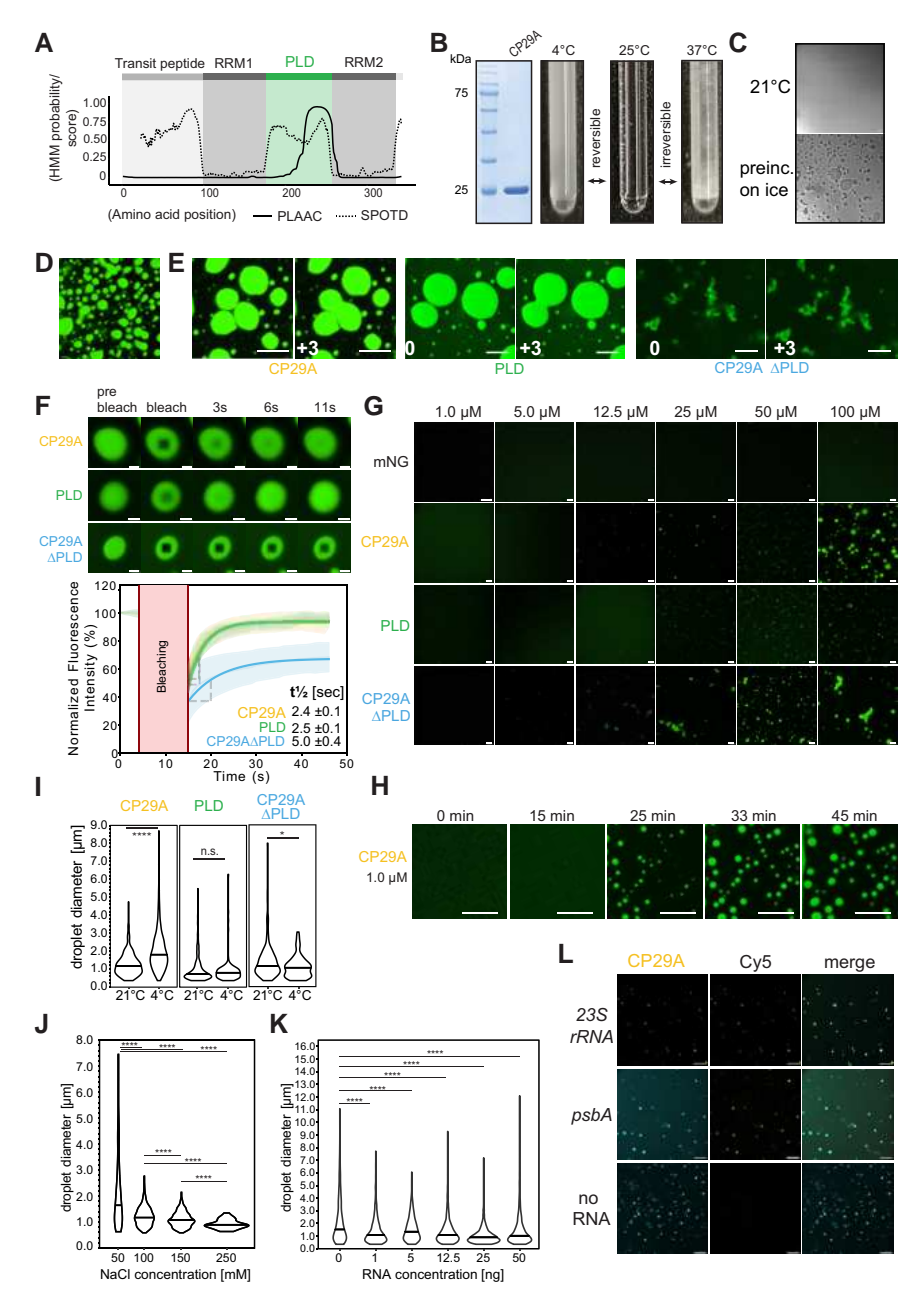


Figure 1. CP29A forms condensates in vitro. A) Schematic diagram of the CP29A protein with its two RRM domains. Below, results of disordered domain predictions within CP29A using the PLAAC and SpotD tools are shown. Scores for both predictors suggest disorderedness in the linker between the two RRM domains, including a predicted PLD. **B)** Left: Coomassie stain of purified recombinant CP29A excluding the signal peptide, separated by SDS–PAGE. Right: Glass vial with 80 µm CP29A solution is shifted between different temperatures to demonstrate reversible turbidity changes. C) PS of nontagged CP29A protein. Solution (50 μm) of full-length CP29A was either kept at 21°C or was incubated for 5 min on ice in the absence of crowding reagent. The solution was analyzed by bright-field microscopy; scale bar = 5 µm. D) In vitro PS assay of 100 µm mNG-CP29A with 10% (w/v) PEG8000 treatment for 1 min prior to imaging; imaged with confocal microscopy, selecting a field-of-view with many merging droplets. scale bar = $5 \mu m$. E) Fusion events of mNG-CP29A and mNG-PLD droplets; conditions as in (C); numbers indicate seconds passed between frames shown; protein concentration: 100 μm; note that CP29AAPLD forms aggregates that were never observed to fuse. scale bar = 5 µm. F) Quantification of FRAP kinetics with mNG-CP29A, mNG-CP29AΔPLD, and mNG-PLD; all at 100 μm. Top: representative images from FRAP movies for the three recombinant proteins. Scale bar: 2 μm. Bottom: quantification of fluorescence recovery. Data are means of the fluorescence values from at least 11 experiments per protein. The images were taken every second over 40 to 50 s to document fluorescence recovery, each time point was normalized to the value before photobleaching; note that the full-length protein and the PLD recover at a very similar rate, while the PLD-less protein recovers much more slowly. Triangles to calculate half live are shown—details on values are shown in Supplementary Table S1. The error (standard deviation) is shown as a shaded tube behind each curve. G) PS of mNG-CP29A, mNG-PLD droplets, and mNG-CP29AAPLD at different protein concentrations, 5 min after adding PEG to a final concentration of 10%; scale bar: 20 µm. The experiment was performed three times; representative results are shown. H) PS of 1 µm mNG-CP29A with 10%PEG (final concentration) at 21°C. Pictures were taken of the same field of view over a time course of 45 min; scale bar: 10 µm. I) Microscopy of mNG-CP29A droplets (left) and their size distribution (right) of mNG-CP29A at 21 and 4 °C, respectively (50 µm protein; 50 mm NaCl), scale bar 20 µm. Wilcoxon- $Mann-Whitney \ Test: \ ^{****P} < 0.0001; \ ^*P < 0.05. \ \textbf{\textit{J}}) \ Size \ distribution \ of \ mNG-CP29A \ droplets \ at \ different \ salt \ concentrations. \ Protein \ concentration: 50 \ \mu\text{M};$ Wilcoxon-Mann-Whitney Test: ****P < 0.0001. K) Size distribution of mNG-CP29A droplets at different total plant RNA concentrations. Protein concentration: 50 µm; scale bar: 20 µm. Wilcoxon-Mann-Whitney Test: *P < 0.05, ****P < 0.0001. L) Co-condensation assay of mNG-CP29A with two RNA species. In vitro transcripts representing parts of the chloroplast 23S rRNA as well as the psbA mRNA were labeled with Cy5 and incubated with mNG-CP29A (50 μм) and 10% PEG. Images were taken after five minutes of incubation at 21 °C.

if distanced by a short linker, although we cannot exclude structural effects of the PLD deletion on the RRM domains.

For visualization, we fused the different protein versions N-terminally to mNeonGreen, while omitting the organellartargeting sequence, since it is cleaved off in vivo. We expressed the protein variants in Escherichia coli and purified them (Supplementary Fig. S1B). Indeed, mNeonGreen-CP29A formed spherical liquid droplets and wetted the glass surface after settling to the bottom of the dish (Fig. 1D; Supplementary Video S2). Droplet size increased over time and droplets started to coalesce, which is indicative of the liquid nature of the phase being formed (Fig. 1E). Similarly, the PLD alone assembled droplets that fused, while the PLD-less CP29A protein formed irregularly shaped aggregates that did not show fusion (Fig. 1E). To investigate the dynamics of mNeonGreen-CP29A within droplets, we performed fluorescence recovery after photobleaching (FRAP) experiments. After highintensity laser irradiation, fluorescence recovers with a halftime of 2.49 ± 0.1 s for the full-length protein, and 2.5 ± 0.1 s for PLD alone, while CP29A Δ PLD recovery is much slower (5.0 \pm 0.4 s; Fig. 1F, Supplementary Table S1). Furthermore, CP29AΔPLD aggregates did not show full recovery after photobleaching, but plateaued at 69% demonstrating low mobility of proteins within this phase, while both full length and PLD CP29A showed a recovery of greater than 95% (Fig. 1F).

As anticipated, our results revealed a positive association between droplet formation and protein concentration, as shown in Fig. 1G for both the full-length and PLD-only proteins. The fulllength and PLD-only proteins resulted in spherical droplets while the PLD-less CP29A did show amorphous aggregates at 25 μm and above (Fig. 1G). No granule formation was observed with recombinant mNG alone (Fig. 1G). Droplet formation of the full-length protein was observed down to 1 µM protein concentration, but it took longer for droplets to become visible (Fig. 1H). We also exposed the full-length protein to low temperatures and observed that droplet size and droplet number increased significantly in the cold (4 °C) (Fig. 1I), with a median diameter of 1.2 μ m at 21 °C and 1.4 μ m at 4 °C (n = 473 and n = 1,087 droplets at 21 and 4 °C, respectively). For the PLD-only protein, there was no significant change in droplet size observed, but there were fewer droplets at lower temperatures (n = 435 and n = 134 droplets at 21 and 4 °C, respectively). For the PLD-less protein, there was a marginal decrease in droplet size, barely reaching significance, and a decrease in droplet number in the cold (n = 133 and n = 85 droplets at 21 and 4 °C, respectively; Fig. 11). This suggests that the entire protein is necessary for responding to cold conditions. We next tested the impact of salt on droplet formation and found that concentrations of 100 and 150 mm salt facilitated droplet formation, while droplet size decreased at higher salt concentrations (Fig. 1J). The negative impact of higher salt concentrations on the full-length protein was also observed at low temperatures in turbidity assays (Supplementary Fig. S1C) and can be interpreted as a suppression of intermolecular interactions by electrostatic shielding. Taken together, these data established that CP29A undergoes PS in vitro to form liquid droplets, which depends on its PLD and is supported by low temperatures.

CP29A is an RNA-binding protein, prompting us to conduct experiments to assess the influence of RNA on its PS behavior. Given CP29A's association with a wide variety of RNA molecules, we incubated recombinant mNG-CP29A with varying amounts of plant total RNA. Our observations revealed a decrease in droplet size across all tested RNA concentrations suggesting that RNA alters the condensation dynamics of CP29A (n=[no RNA: 841, 1 ng: 751, 5 ng: 887, 12.5 ng: 1,600, 25 ng: 1,968, 50 ng: 1,406] Fig. 1K).

To determine the potential of droplets to incorporate RNA, we synthesized two in vitro RNA transcripts, labeled them with Cv5, and incubated them with mNG-CP29A. Both RNAs were found to localize within the granules (Fig. 1L), indicating an interaction with CP29A in the condensed phase. Collectively, these analyses indicate that RNA plays a role in modulating the biophysical characteristics of CP29A droplet formation.

NMR analysis of CP29A indicates molecular interactions of the PLD within the condensed phase

Next, we utilized nuclear magnetic resonance (NMR) spectroscopy along with other biophysical methods in order to investigate the conformation of CP29A at residue level. We expressed and purified the individual RRM domains and the PLD linker and assigned the NMR backbone chemical shifts. Our analysis revealed that CP29A harbors two canonical RRM domains with β_1 - α_1 - β_2 - β_3 - α_2 - β_4 - β_5 and β_1 - α_1 - β_2 - β_3 - α_2 - β_4 secondary structure for RRM1 and RRM2, respectively. Furthermore, NMR chemical shifts indicate that the PLD linker connecting the two RRMs is intrinsically disordered (Fig. 2A, Supplementary Fig. S1, B, D, and E). Notably, the PLD linker of CP29A comprises low-complexity regions with repeats of serine (17%), arginine (9%), tyrosine (7%), and glutamate (6%; Fig. 2B, Supplementary Fig. S1A), which can potentially engage in electrostatic and cation- π interactions and is rich in glycines (34%; Fig. 2B). These features can mediate interactions in phase-separated condensates (Wang et al. 2018b; Qamar et al. 2018). To study the PS potential of CP29A in detail, we monitored changes of full length CP29A at temperatures ranging from 298 to 275 K in NMR fingerprint spectra. Extensive line-broadening of amide signals was observed at low temperatures, consistent with reduced molecular tumbling of the protein in a disperse phase (Figs. 1B and 2, C and D). The extent of line-broadening was substantially larger than expected from the temperature dependence of the molecular tumbling, suggesting that it is due to molecular interactions in the condensed phase.

Since the PLD linker is responsible for PS of CP29A (Fig. 1), we purified the PLD alone and analyzed its biophysical properties (Fig. 2E; Supplementary Fig. S1, B and D middle panel). By lowering the temperature from 289 K/25 °C to 275 K/2 °C, noticeable line-broadening of amide signals was observed, similar to with the full-length protein, consistent with reduced mobility and condensate formation in disperse solution (Fig. 2, F and G upper panel). To investigate the conformational dynamics of the PLD in solution, {1H}-15N heteronuclear nuclear Overhauser effect (hetNOE) experiments were performed at 298 K/25 °C and 275 K/2 °C. These data demonstrate that the PLD has overall reduced backbone flexibility at subnanosecond time scales at low temperature with pronounced rigidification for glycines and serines between residues 245 and 254 (Fig. 2G, lower panel). The overall flexibility of the PLD is also seen in a Kratky plot derived from small-angle X-ray scattering (SAXS; Supplementary Fig. S2A). The pairwise-distance distribution suggests a broad range of conformations of the protein up to 100 $\hbox{\normalfont\AA}$ pairwise distances, indicating that the PLD dynamically samples a wide range of conformations in solution (Supplementary Fig. S2, B to F; Supplementary Table S2). This behavior is consistent across both NMR and SAXS buffer salt concentrations (Supplementary Fig. S2, G and H). In summary, the low complexity region of the PLD of CP29A is unstructured, flexible, and undergoes temperaturedependent PS similar to previously characterized PLDs (Wang et al. 2018b; Franzmann and Alberti 2019).

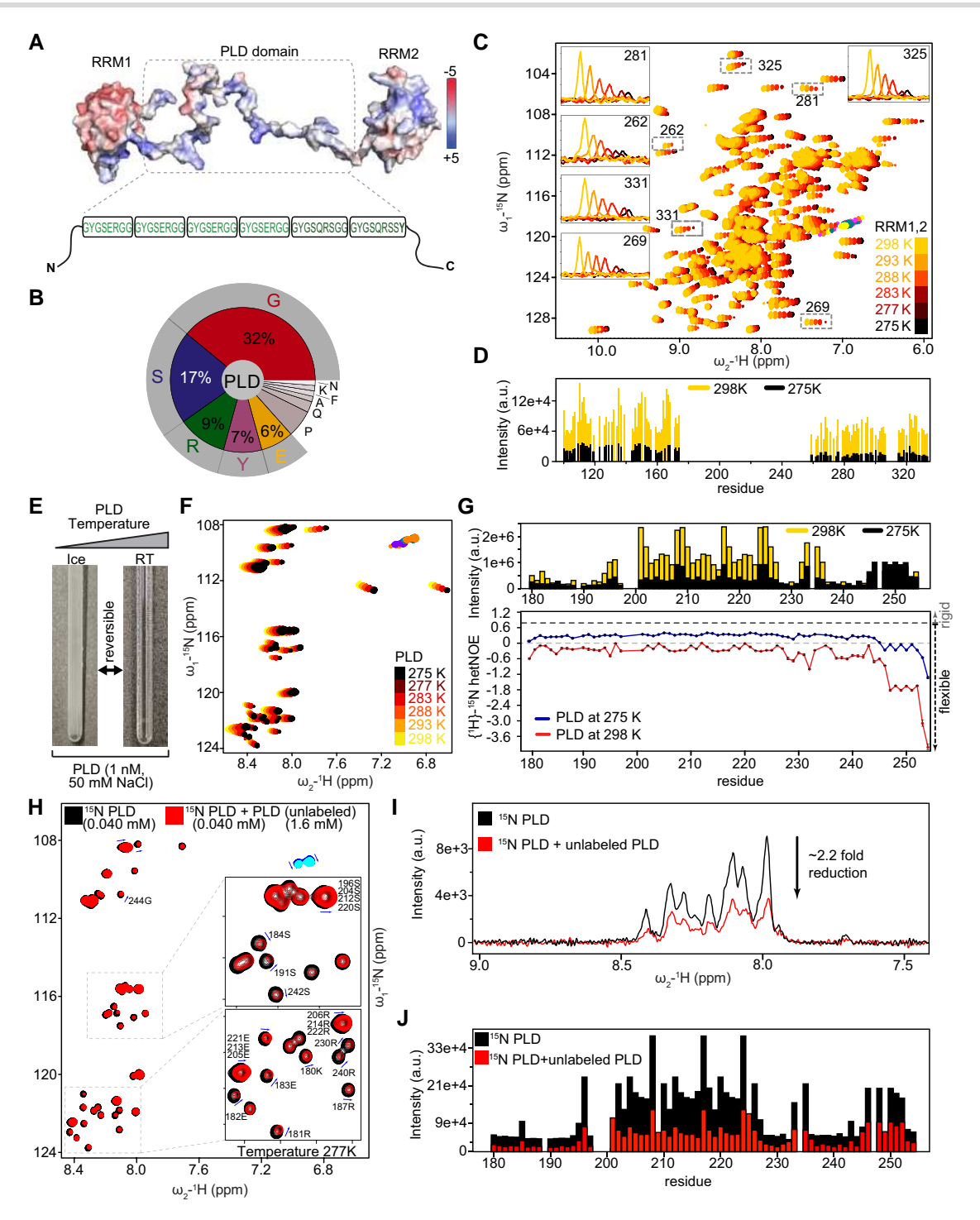


Figure 2. Temperature dependent biophysical characterization of tandem RRMs and the PLD linker of CP29A. A) Structural model of tandem RRMs of CP29A with electrostatic surface potential rendering (kJ/mol/e) and the primary sequence of its PLD linker. Repeated sequence elements are boxed. B) Pie-chart shown for the PLD domain with the proportion of each amino acid. C) Overlay of ¹H, ¹⁵N NMR HSQC spectra of 90 μM concentration of tandem RRMs of CP29A measured at different temperatures. The inset shows the line-broadening with 1D slices of the cross peaks in the 2D experiment upon temperature shift from 298 to 275 K. D) Boxplot for signal intensities of amide protons for spectra shown in (C) at 298 K (yellow) and at 275 K (black). E) Turbidity changes of a 1 mM PLD solution upon change from ice to room temperature. F) Overlay of a series of ¹H, ¹⁵N HSQC spectra of the PLD linker with increasing temperature from 275 to 298 K. Line-broadening of NMR signals is observed at 275 and 277 K. G) Upper panel: Box plot of the intensity of amide proton signals in (F) at 298 and 275 K, in yellow and black color, respectively. Lower panel: Comparison of (¹H)-¹⁵N heteronuclear NOE of the PLD at 298 and 277 K shown in red and blue, respectively. H) Overlay spectra of the ¹⁵N labeled PLD alone (black) and in presence of 40-fold excess of unlabeled PLD (red) measured at 277 K. Blue arrows indicate small chemical shift changes. I) Overlay of 1D amide proton signals for the samples and conditions shown in figure (H). Intensity reduction of the signals is indicated with an arrow. J) Box plot for signal intensities in the spectra shown in (H).

To confirm that the observed NMR line-broadening reflects reduced tumbling in the condensed phase based on intermolecular interactions, we conducted an NMR titration of ¹⁵N-labeled PLD

with unlabeled PLD at low temperature (4 °C; Fig. 2, H and I). Changes in amide chemical shifts and line-broadening, reflected by a 2.2-fold intensity reduction upon the addition of 40-fold

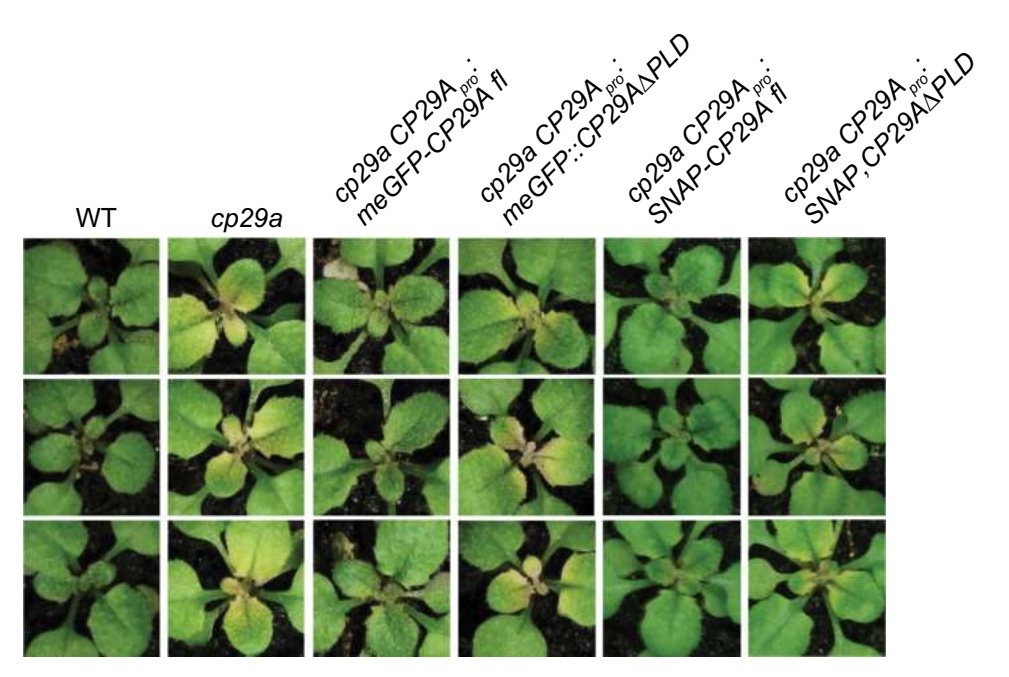


Figure 3. Phenotype of wt, cp29a mutants and complementation lines after 14 d at 21 °C and 14 d at 8 °C.

molar excess of unlabeled PLD protein, suggested that the ¹⁵N-labeled protein participates in PS with the unlabeled protein in a condensed phase. The most prominent NMR spectral changes were observed for the Gly-Tyr-Gly-Ser-Glu-Arg-Gly-Gly repeats, consistent with weak electrostatic intermolecular interactions (Fig. 2J). In summary, our NMR analysis demonstrates high flexibility of the PLD in free solution, which is reduced at low temperatures consistent with charged interactions that contribute to condensed phase formation.

The PLD is required for plant cold resistance

Null mutants of CP29A show pale tissue at the center of the leaf rosette after longer cold exposure, a phenotype that is reversible when plants are returned to normal growth temperatures (Supplementary Fig. S3), well in line with the reversible nature of the CP29A phase-separation event observed in vitro (Fig. 1B). We next tested whether the PLD is required for CP29A-mediated cold resistance. To this end, we generated plant lines that express meGFP fused to full-length CP29A (CP29Apro:meGFP-CP29Afl), and CP29A without its PLD (CP29Anno:meGFP-CP29AAPLD), both in a cp29a null mutant background. We also generated plants with an N-terminal SNAP-tag in the same background (CP29Apro: SNAP-CP29Afl and CP29A_{pro}:SNAP-CP29A_APLD). The expression of all constructs was driven by the native CP29A promoter, and their expression levels were compared to the wt (Supplementary Fig. S4, A and B). We exposed 14-d-old plants from all transgenic lines to 8 °C for 14 d. The plants expressing full-length CP29A remained green under these conditions, no matter which fluorescent tag was used, demonstrating that the N-terminal fusion protein could functionally replace the wt protein (Fig. 3). By contrast, plants expressing PLD-less protein versions showed a pale center of the rosette, although the affected area appeared smaller than in null mutants and the extent of paleness varied between different individual plants (Fig. 3). This demonstrates that the CP29AAPLD is not capable of fully reverting the mutant phenotype and only leads to a partial

complementation. We conclude that the PLD of CP29A is required for cold-resistance.

CP29A localizes to granules proximal to nucleoids in vivo

We next investigated the potential of CP29A to undergo PS within plant chloroplasts. We prepared protoplasts from these plants and conducted microscopic analyses at 8 °C. This temperature, milder than the in vitro extreme cold stress of 4 °C, was chosen to more closely resemble the conditions commonly encountered in natural environments. Protoplasts from the CP29Apro:meGFP-CP29Afl lines exhibited punctate signals when analyzed by confocal microscopy, which increased in number over time when incubated at 8 °C, while protoplasts from the CP29Apro:meGFP-CP29AAPLD plant lines showed much fewer granular signals (Fig. 4A). These findings suggest that the PLD of CP29A is strongly supportive of efficient droplet formation in vivo, but also shows that recruitment into granular structures is still possible for the truncated CP29A protein albeit at much lower efficiency. Furthermore, our data indicate that low temperatures not only promote droplet formation in vitro but also in living cells.

We next investigated whether the formation of CP29A droplets is linked to nucleoids, given that nucleoids contain a large number of RNA-binding proteins (Majeran et al. 2011). To answer this question, we utilized STED microscopy, which is better equipped to resolve the suborganellar distribution of CP29A droplets and DAPI-stained nucleoids than standard confocal microscopy. Our observations indicated that the GFP signal and the DAPI signal only occasionally overlap (Fig. 4B). However, we frequently observed that the two signals appeared as doublets (Fig. 4B, arrowheads), prompting us to explore the possibility of a physical connection between CP29A droplets and nucleoids, similar to the known tethering of mitochondrial RNA droplets to nucleoids (Rey et al. 2020; Antonicka and Shoubridge 2015). By measuring the distance between nucleoids and CP29A droplets, we discovered a nonrandom distribution of the two signals, with

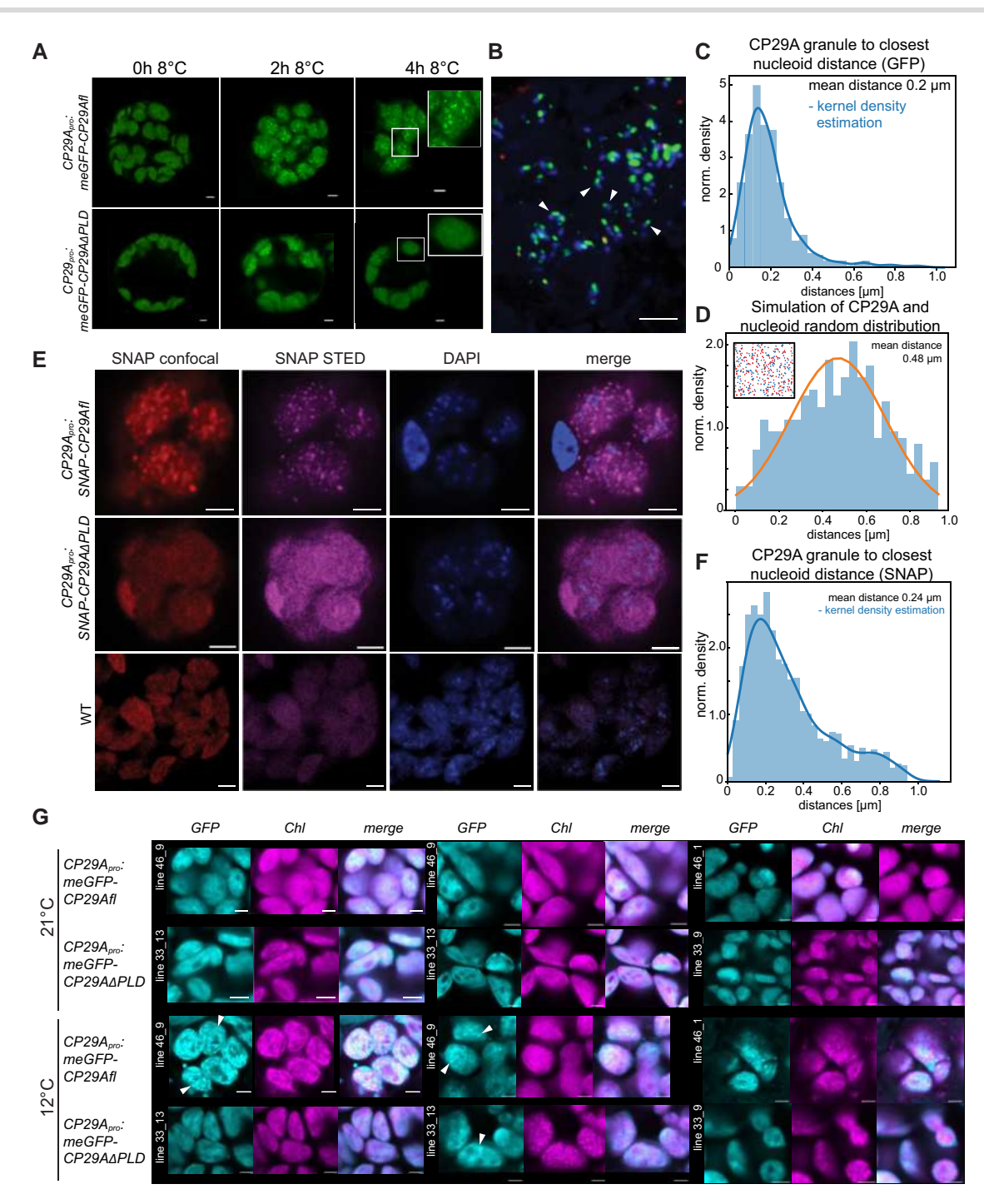


Figure 4. CP29A forms droplets in the vicinity of nucleoids, which depends on its PLD and is fostered by low temperatures. **A)** Confocal microscopy of protoplasts prepared from wt and the transgenic cp29a lines stably expressing CP29Apro:meGFP-CP29Afl or CP29Apro:meGFP-CP29AdPLD, exposed to low temperature for the indicated time. Scale bar: 10 μm. Three replicates were performed with independent transgenic lines for each genotype, imaging between 24 and 36 protoplasts per genotype. **B)** Leica STED microscopy of protoplasts from cp29a; CP29Apro:meGFP-CP29Afl plants, incubated for 1 h at 8 °C and stained with DAPI. Arrowheads point to examples of doublet signals. Scale bar = 1 μm. **C)** Quantification of the distance of CP29A droplets and nucleoids in (**B)**. **D)** Simulation of a random distribution of CP29A droplets and nucleoids based on the number of signals in (**B)** per volume analyzed. **E)** Confocal and STED microscopy of protoplasts prepared from transgenic cp29a lines stably expressing CP29Apro:SNAP-CP29Afl or CP29Apro:SNAP-CP29AAPLD and exposed to 8 °C for 1 h. Scale bar: 10 μm. **F)** Quantification of the distance of CP29A droplets and nucleoids in (**E)**. **G)** Subcellular localization of meGFP-CP29Afl or meGFP-CP29AAPLD was observed both at standard growth temperatures and after cold acclimation. For each construct, we analyzed two distinct independent lines (indicated by line numbers in white font). Depending on the line, either one or two sets of images are presented. Each set includes separate images for the GFP channel and the chlorophyll autofluorescence channel, along with a merged image of the two. Some granules are highlighted with arrowheads in the images. Scale bar: 2 μm.

an average distance of 0.2 μ m (Fig. 4C). As a control, we examined whether a modeled random distribution of nucleoids and CP29A droplets would result in a similar distance. For that we estimated average numbers of nucleoids and CP29A

droplets from fluorescence images and found that a random distribution of the two signals in the chloroplast volume led to an average distance of 0.488 μ m, which was substantially larger than the distance measured in the in vivo data (Fig. 4D).

To validate our findings using an alternative detection method of CP29A droplets, we employed the SNAP tag, which is also more suitable for STED microscopy since it allows the usage of organic dyes that emit two orders of magnitude more photons than GFP (Fernández-Suárez and Ting 2008; Dempsey et al. 2011). We generated protoplasts from both CP29Apro: SNAP-CP29Afl and CP29Apro:SNAP-CP29AAPLD lines and incubated them with the SNAP-compatible dye Cell-SiR647 for 1 h. As seen in the CP29Apro:meGFP-CP29A expressing plants, only the lines expressing full-length CP29A exhibited a granular localization of CP29A, while the plants lacking the PLD showed a diffuse signal with few granular bodies (Fig. 4E). Consistent with our observations in GFP-tagged lines, we also found an association between the location of CP29A signal and nucleoids in CP29Apro:SNAP-CP29Afl protoplasts (Fig. 4F), with an average distance of the two signals of 0.24 µm. These findings demonstrate that droplet formation occurs in living chloroplasts and is not reliant on the tags utilized, as both GFP- and SNAP-tagged CP29A form droplets. Moreover, our results provide compelling evidence that CP29A droplets are in close proximity to nucleoids.

To further corroborate our findings, we performed immunofluorescence assays on wt protoplasts using an antibody against the native CP29A protein. Since the antibody was designed to recognize the PLD region, it could only be used for analysis of plants expressing full-length CP29A. Consistent with our GFPand SNAP-tagged fusion protein experiments, immunofluorescence assays revealed granular signals that increased in number at low temperatures (8 °C, Supplementary Fig. S5A). We observed that the granular signals were mainly located near the chloroplast envelope, potentially due to limitations in the antibody's ability to penetrate formaldehyde-fixed chloroplasts densely packed with thylakoid membranes. Importantly, this analysis demonstrates that droplet formation of CP29A is not an artifact of transgene overexpression or fusion protein production.

To exclude that granule formation is induced by protoplastation, we next investigated leaf tissue for the localization of meGFP-CP29Afl and meGFP-CP29AAPLD. Starting with material grown entirely at 21 °C, we saw very few granular structures in chloroplasts of either genotype (Fig. 4G). When the plant material was however transferred to 12 °C, the signals became more punctate in CP29Apro:meGFP:CP29Afl plants. These signals were not in all cases roundish, possibly restricted and deformed by the thylakoid membrane system. The GFP signal is still distinct and does rarely overlap with the red chlorophyll signal. In some instances, the red chlorophyll signal exhibits a dotted pattern, indicative of grana membrane stacks, as seen for example in line 33 to 13 at 12 °C (refer to the middle panel in Fig. 4G); however, these red thylakoid dots do not overlap with the GFP signal, in line with CP29A being a soluble protein. In some CP29Apro:meGFP-CP29Afl cells, chloroplasts were replete with granules. Structures with higher signal density were also found in chloroplasts from CP29Apro:meGFP-CP29AdPLD leaves, but in much lower numbers (Fig. 4G). We also conducted FRAP on CP29Apro:meGFP-CP29Afl to evaluate fluidity. However, this resulted in the rupture of chloroplasts, likely due to excessive energy transfer through chlorophyll (see Supplementary Fig. S5, B to D). Consequently, we cannot currently confirm whether the granular structures observed in vivo are liquid-like. Taken together, our analyses provide strong evidence that CP29A forms droplets near nucleoids in living cells. Reflecting our findings in vitro, granule formation is strongly supported by the PLD region and is promoted by low temperatures.

Chloroplast RNA splicing defects in long-term cold-treated cp29a mutants

To understand the molecular function of CP29A in the cold, we initially sequenced RNA from long-term cold-treated mutant plants and compared it to wt plants to get transcriptome-wide insights into potential gene expression defects. We used young plants, 5 d after germination, since the macroscopic phenotype is restricted to young, emerging tissue. These plants were then kept at 8 °C for 16 d, during which time the plants hardly grew. Since the chlorotic, cold-dependent phenotypic defect is present in newly developing leaf tissue only, the nonbleached green cotyledons were removed prior to sampling triplicates. RNA was extracted and ribosomal RNAs were depleted prior to Illumina-based sequencing. A principal component analysis was used to ensure the concordance between replicates and experimental groups (Supplementary Fig. S6A). The comparison of the wt plants grown at low temperatures versus cp29a mutant plants grown at low temperatures, showed 661 differentially expressed nuclear genes (DEGs), most of them downregulated in the mutant (Supplementary Fig. S6B). Among the downregulated genes were many photosynthesis-associated nuclear genes (PhANGs). PhANG expression is specifically downregulated at 21 °C versus 8 °C in mutants, but not in wt, a case in point being the genes for subunits of the light harvesting complexes (LHCs) and photosystems (Supplementary Fig. S6, B and C). This is unsurprising, since defects in chloroplast biogenesis are known to induce the reduction of PhANG expression to avoid wasteful protein production when there are problems with chloroplast development (Richter et al. 2023; Liebers et al. 2022). Or in other words, the effects we observed can be explained by the strong chloroplast developmental phenotype and are thus very likely secondary. We noticed, however, an interesting change in splicing efficiency of chloroplast introns in the RNA-seq dataset. The Arabidopsis chloroplast genome contains 21 introns and we tested their splicing efficiency by comparing reads across exon-exon borders versus reads crossing intron-exon borders (introns in tRNAs could not be assessed because their short exons did not allow the detection of intron-exon spanning reads). We obtained splicing efficiency measurements for 15 introns. With the exception of the intron in rps16, which is a pseudogene in Arabidopsis and not spliced (Ueda et al. 2008; Roy et al. 2010). Splicing was significantly reduced for all introns in cold-treated cp29a mutants (Fig. 5A).

Short-term cold-treated plants neither display chloroplast development defects nor differential chloroplast RNA accumulation

To investigate the onset of molecular defects in the cp29a mutant after cold treatment and to avoid measuring secondary effects due to leaf bleaching, we analyzed plants that were exposed to low temperatures for shorter periods. To this end, we harvested tissue that had been grown for 14 d at 21 °C and then moved to 12 °C for 3 and 10 d, respectively. We used 12 °C instead of 8 °C to further reduce the detrimental bleaching effects at even lower temperatures. After 3 and 10 d in the cold, we observed no macroscopic differences between the cp29a mutant plants, wt plants and the complementation lines (Supplementary Fig. S7A). To assess the potential occurrence of electron transport problems in the thylakoid membrane after cold treatment, we assayed chlorophyll fluorescence using pulse amplitude modulated fluorescence measurements (PAM). The PAM technique essentially measures changes in PSII photochemical efficiency (in the dark-adapted state), which provides an indicator of electron transport problems in the thylakoid membrane. In long-term treated tissue, cp29a mutant plants exhibited a marked increase

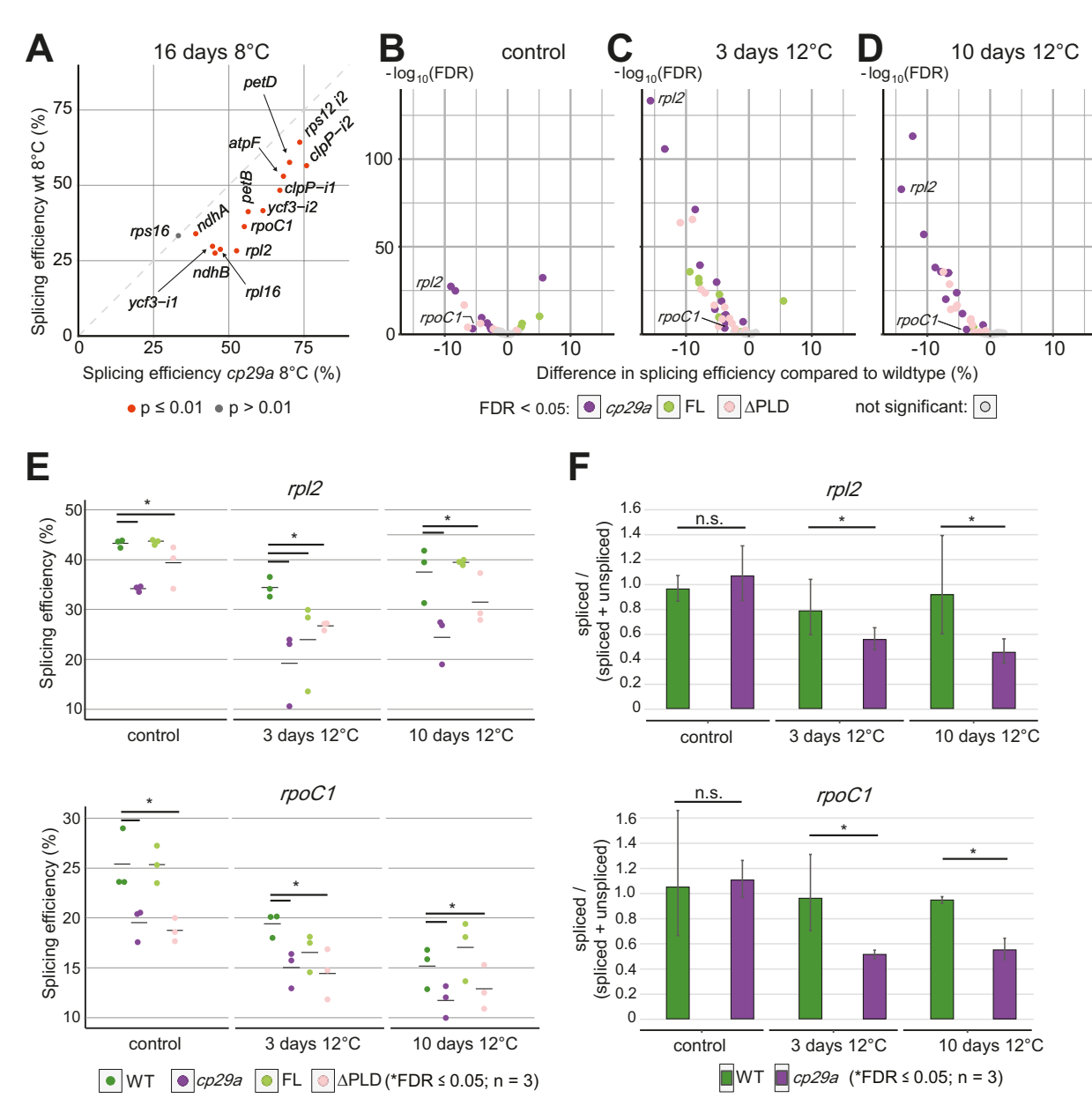


Figure 5. Splicing of chloroplast group II introns in the cold depends on CP29A's PLD. A) Analysis of splicing efficiency of chloroplast introns in long-term cold-treated wt and cp29a mutant plants by RNA-seq. Splicing efficiency was calculated as the ratio of reads spanning exon–exon junctions versus reads spanning intron–exon boundaries (Castandet et al. 2016). B) Analysis of splicing efficiency by RNA-seq after plant growth for 12 d under standard growth conditions in cp29a null mutants, wt and complementation lines plus. As indicated below the graphs, dots represent introns with significantly changed RNA splicing in the different genotypes (FDR > 5). C) Same analysis as in (B) after 12 d at normal temperature and 3 d of cold treatment at 12 °C. D) Same analysis as in (B) after 11 d at normal temperature and 10 d at 12 °C. E) Analysis of RNA-seq data described in (C) to (E) specifically for the splicing efficiency of rpl2 and rpoC1 mRNAs. Bars indicate the mean of the three replicates. F) Analysis of splicing of rpl2 and rpoC1 in wt and cp29a mutants after 3 and 10 d at 12 °C by RT-qPCR. PCR products were either spanning exon–exon junctions ("spliced") or exon–intron junctions ("unspliced") and splicing efficiency was calculated as the ratio of qPCR-signals of spliced amplicons over the sum of signal for spliced and unspliced amplicons. Error bars represent the 95% confidence interval for relative quantification (RQ), indicating the range from RQmin to RQmax.

in fluorescence at the center of the rosette, indicating that normal electron transport in the thylakoid membrane is disturbed (Supplementary Fig. S7B). However, this phenotype was absent in plants exposed to cold for 3 d, and only a slight increase in fluorescence was measured in *cp29a* plants that were cold-treated for 10 d (Supplementary Fig. S7A).

We then harvested the three youngest leaves, extracted total RNA, depleted rRNA, and performed RNA sequencing in biological triplicates. Principal component analysis (PCA) showed that the three biological replicates of each treatment consistently

clustered together, while the four genotypes were similar under control conditions but dissimilar after 10 d of cold treatment (Supplementary Fig. S7C). This supports the idea that expression differences between cp29a mutants and wt plants occur only in the cold and increase over time. One replicate of the cp29a mutant after 10 d in the cold and one wt plant after 3 d in the cold seemed closer to the other replicates. However, it is important to note that a greater difference in biological characteristics between samples can occur due to either uncontrolled environmental factors or inherent variations in plant growth.

To investigate potential defects in chloroplast gene expression, we compared the wt, mutant, and complemented mutant samples exposed to the same low temperature regime (12 °C). Firstly, we looked for differences in chloroplast RNA accumulation, but found none in this short-term cold-treated material, including mRNAs for components of the photosynthetic machinery (Supplementary Fig. S7D). This is in contrast to long-term cold-treated mutant tissue, where many photosynthesis-related mRNAs are reduced relative to wt (Supplementary Fig. S6, B and C). This analysis demonstrated that the secondary, pleiotropic effects observed in long-term cold-treated cp29a plants at 8 °C had not yet manifested after short-term 12 °C treatment and that altered chloroplast RNA accumulation is not an early effect in the mutant in the cold.

Splicing in short-term cold-treated tissue depends on CP29A's PLD

To investigate splicing defects in short-term cold-treated plants (12 °C), we analyzed splicing efficiency in our RNA-seq dataset. Even without cold treatment, there were already several introns with significantly reduced splicing efficiencies in the null mutants and Δ PLD plants relative to wt (Fig. 5B). No reduction in splicing was observed in the full-length complementation line, but three introns showed increased splicing efficiency. After 3 d in the cold, the number of introns with significantly reduced splicing efficiency increased in null mutants from 7 to 12 and in Δ PLD complementation lines from 5 to 12 (Fig. 5C). Not only did the number of deficiently spliced introns increase, but the strength of their defects also increased in the cold compared to in normal temperatures. Unexpectedly, the full-length complementation line exhibited splicing defects after 3 d in the cold, albeit to a lesser extent than the null mutant and the Δ PLD line. However, these defects disappeared after 10 d in the cold, when only one intron showed significantly reduced splicing in full-length complementation lines (Fig. 5D). Given that the full-length construct nearly fully complemented the null mutation after 10 d in the cold, we speculate that the changes in splicing seen at normal temperatures and at 3 d cold exposure are caused by expression differences of the transgene relative to the endogenous CP29A gene. The genomic location of the construct cannot be controlled by the transformation method used, and thus, despite using the same native promoter for all transgenic lines, different expression patterns can occur.

The PLD-less version of CP29A, in contrast to the full-length construct, still exhibited pronounced splicing defects after 10 d of cold treatment (12 °C; Fig. 5D). The defects were not as strong as in the null mutant, indicating that partial complementation of the splicing defect occurs. These findings were also visualized by comparing splicing efficiency of individual introns. For this, we chose rpl2, because it showed the strongest reduction in splicing efficiency in the cp29a null mutant (Fig. 5, C and D). rpl2 encodes a subunit of the chloroplast ribosome, which is essential for chloroplast development (Zoschke and Bock 2018). We also added rpoC1 to the analysis since its gene product is part of an essential chloroplast gene expression machine, the plastid-encoded RNA polymerase (Hajdukiewicz et al. 1997), and is an example of a gene with a milder splicing deficiency in our RNA-seq experiment (Fig. 5, C and D). For both introns, the ΔPLD line can only partially complement the splicing defect of the null mutant (Fig. 5E). We validated these RNA-seq results by analyzing splicing of rpl2 and rpoC1 via RT-qPCR. By amplifying spliced versus unspliced mRNAs, we confirmed the splicing defects of both transcripts in the null mutant (Fig. 5F). Overall, our analysis demonstrates that shortcomings in chloroplast splicing are early defects in the *cp29a* mutant after cold exposure and that the PLD is required for full splicing capability in the cold.

Ribosome profiling of *cp29a* mutants suggests a global reduction of chloroplast translation after short-term cold-treatment

Given that several introns with reduced splicing are in genes coding for ribosomal proteins, including rpl2, we hypothesized that cp29a mutants may have translation defects in chloroplasts after cold exposure. We therefore used ribosome profiling (Ribo-seq) in cp29a mutants and wt to assess translation. Wild type and cp29a null mutants were grown for 15 d at 21 °C and then shifted to 12 °C for 3 d (in three biological replicates). Like in the RNA-seq assays discussed above, the rationale behind this short and mild cold treatment was that we avoid pleiotropic effects of the bleaching phenotype after long-term cold treatment of tissue. Whole leaf tissue was processed for Ribo-seq analysis as well as for parallel RNA-seq. Ribosomal RNA was depleted from all libraries. Ribo-seq reads mapping to the chloroplast displayed the previously described broad size distribution (Chotewutmontri and Barkan 2016), whereas reads mapping to nuclear genes resulted in the expected narrower size distribution for cytosolic ribosomes, peaking at 29 nt (Supplementary Fig. S8A). The footprints mapped predominantly to coding regions, where they show the expected periodicity and preference for the first reading frame, (Supplementary Fig. S8B). The Ribo-seq and RNA-seq RPKM values showed a high level of consistency between the replicates (Supplementary Fig. S8, C and D), with each replicate comprising at least 2 million Ribo-seq reads and 4 million RNA-seq reads mapping to the chloroplast transcriptome (Supplementary Table S3).

Standard Ribo-seq and RNA-seq analyses usually rely on detecting a limited number of transcript changes in a large set of transcripts, of which the majority remains unchanged between conditions and genotypes. In a small transcriptome like the chloroplast, a general effect on translation is expected to affect the majority, if not all, of the 80 protein-coding transcripts. Standard normalization of individual sequencing libraries for chloroplast sequencing depth would mask any such general effect. To address this, we compared all chloroplast reads in a sample with all nuclear reads across replicates, thus performing a sample-internal normalization against the nuclear ribosome footprints. This analysis revealed a significant global reduction in chloroplast ribosome footprints in cold-treated mutants versus cold-treated wt and the analysis of individual genes like rpl2 confirmed this effect (Fig. 6A). In contrast, a parallel comparison of the RNA-seq reads from chloroplasts versus nuclear reads did not show a global change in transcript abundance in the mutant nor of rpl2 (Fig. 6B). This is consistent with our RNA-seq results from shortterm cold-treated mutants and complementation lines: There were no differences in chloroplast RNA accumulation after 3 and 10 d of cold between wt and cp29a mutants and there were only a handful of nuclear transcript changes in these libraries (Supplementary Fig. S7D). Similarly, there were no changes in chloroplast transcript abundance and few changes in nuclear transcripts between complementation lines using the full-length CP29A or a PLD-less version of the protein after short-term cold treatment (Supplementary Fig. S8D). These results suggest that the reduction in translation observed is not caused by a destabilization of chloroplast transcripts. Therefore, we conclude that translation is globally reduced in cp29a cold-treated mutants,

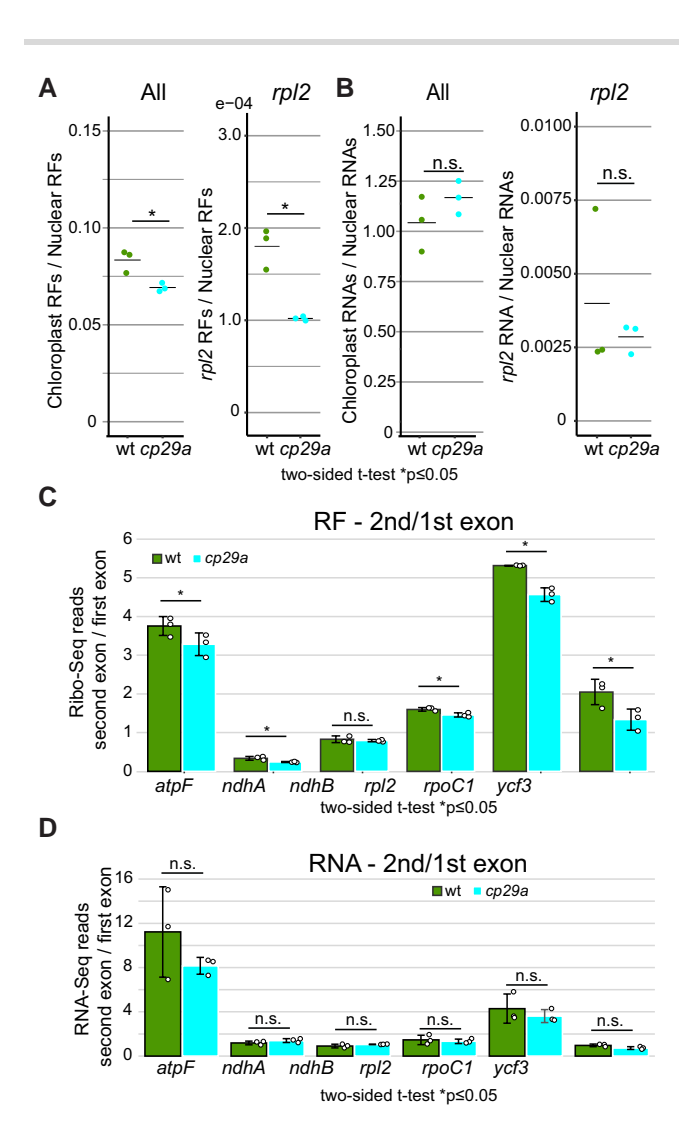


Figure 6. Ribosome profiling and RNA sequencing of short-term cold-treated mutants versus wt. A) The ratio of ribosome footprints from chloroplast versus nuclear mRNAs is shown for cold-treated (12 °C—3 d) wt and cp29a mutant plants. Left: analysis of RF reads from all chloroplast genes normalized to all nuclear RF reads. Right: analysis of RF reads mapping to chloroplast rpl2 normalized to all nuclear RF reads. The ratios of three individual biological replicates are shown as black dots. Bars indicate the mean of the three replicates. Two-sided t-tests; *P \leq 0.0501, n = 3. **B)** The ratio of RNA-seq reads for chloroplast and nuclear mRNAs based on RNA preparations from the same batch of plants as in (A). Left: analysis of RNA-seq reads from all chloroplast genes normalized to all nuclear reads. Right: analysis of RNA-seq reads mapping to chloroplast rpl2 normalized to all nuclear reads. Bars indicate the mean of the three replicates. Two-sided t-tests; *P \leq 0.05, n = 3. **C)** Analysis of splicing efficiency in Ribo-seq data by calculating the ratio of Ribo-seq reads in the second over the first exon of the chloroplast mRNAs. Two-sided t-tests *P ≤0.05. Circles indicate the individual replicates. D) Analysis of splicing efficiency in RNA-seq data analogous to (C).

likely contributing to the defects in chloroplast biogenesis observed after long-term cold treatment.

Ribosome occupancy can serve as a readout for splicing efficiency in chloroplasts since, unlike in the nucleo-cytosolic compartment, translation, and splicing are not separated (Zoschke et al. 2013; Zoschke and Bock 2018). As a result of a splicing defect, ribosomes accumulate in the first exon but cannot reach the second exon in unspliced chloroplast mRNAs. Thus, the second-to-first exon read ratio is informative for splicing efficiency. We tested this for all chloroplast introns that had at least 50 reads per adjacent exon.

We found a significant reduction in Ribo-seq reads for the second-exon-over-first-exon ratio for five out of six introncontaining mRNAs in cold-treated mutants compared to wt samples (Fig. 6C). In contrast, RNA-seq data showed no significant change in RNA coverage between the second and first exon for the same intron-containing genes (Fig. 6D). This further supports the requirement of CP29A for efficient splicing of chloroplast introns early after cold treatment. In summary, Ribo-seq reveals that both splicing and translation are reduced in 3-d cold-treated mutants.

Discussion

The PLD of CP29A is required for efficient chloroplast RNA splicing in the cold

We established that the chloroplast RNA-binding protein CP29A forms droplet-like structures within chloroplasts, which are more prominent in cold conditions. These droplets rely on the presence of the PLD in CP29A, suggesting that they form through PS. This is consistent with what we observed in vitro and based on our NMR analysis of full-length and PLD-only proteins. Our analyses of cp29a mutants and complementation lines revealed reduced splicing efficiency after cold exposure. Even at normal growth temperatures, we observed minor but significant splicing issues. While splicing is not completely lost in null mutants and Δ PLD mutants after cold treatment, it is noticeably reduced. Based on our findings, we propose several possible explanations for the splicing defect.

Firstly, CP29A may directly act as a splicing factor for chloroplast introns. These introns belong to bacterial group II introns, which require complex 3D structures for proper splicing (Zhao and Pyle 2017). Previous studies have shown that low temperatures can hinder group II splicing by disrupting the intron's internal interactions (Dong et al. 2020). We suspect that kinetic traps stabilize alternative RNA structures, which are not biologically functional and impede splicing. In bacteria, RNA-binding proteins can aid correct RNA folding at low temperatures (Lindquist and Mertens 2018), and bacterial intron maturases can rescue splicing of bacterial introns in the cold (Dong et al. 2020). CP29A may fulfill a similar role by directly interacting with the intron and acting as an RNA chaperone. Arabidopsis CP29A was found to associate with most chloroplast mRNAs in RIP-chip experiments (Kupsch et al. 2012), but a preference for introns was not reported. Relatives of CP29A in tobacco (N. tabacum) showed a preference for unspliced RNAs in co-immunoprecipitation experiments (Nakamura et al. 1999), and were shown to directly bind RNA in vitro (Li and Sugiura 1991; Ye and Sugiura 1992). Thus, a direct role of CP29A acting as an RNA chaperone cannot be ruled out at present, but our finding that CP29A forms condensates also supports an alternative mechanism.

Recent studies provide evidence supporting the functional significance of condensate formation in RNA processing. These studies demonstrate that modifying or eliminating protein domains that facilitate PS in RNA-binding proteins (RBPs) can impact mRNA maturation (Gueroussov et al. 2017; Ying et al. 2017; Wang et al. 2018a; Li et al. 2020). This phenomenon has also been observed in splicing. Both RBFOX1 and members of the hnRNP A/D family promote splicing of their target RNAs through condensate formation mediated by intrinsically disordered regions (IDR; Gueroussov et al. 2017; Ying et al. 2017). Similarly, the PLD of the Arabidopsis flowering control locus A (FCA) facilitates the creation of nuclear phase-separated bodies that enhance the polyadenylation of target RNAs (Fang et al. 2019). Phase-separated compartments involved in RNA maturation often exhibit higher concentrations of the associated components compared to the noncondensed phase. Such an increase in

the concentration of splicing factors would promote the splicing reaction. Chloroplast introns always depend on sets of splicing factors that have overlapping, but not fully redundant intron specificities (recently reviewed in Lee and Kang 2020; Wang et al. 2022). Speculatively, these chloroplast RNA splicing factors are recruited to CP29A droplets, thus locally enhancing their concentration in the presence of nascent transcripts from the nucleoid. Future cataloging of the components of the CP29A droplets has the potential to determine whether other known chloroplast splicing factors are enriched in the condensed phase.

Early splicing and translation defects explain impaired chloroplast biogenesis in cold-treated cp29a mutants

The first molecular abnormalities observed in cp29a mutants after exposure to cold temperatures are a decrease in splicing efficiency and reduced ribosome occupancy of chloroplast mRNAs. These changes occur before any visible effects on photosynthesis and chloroplast development. Conversely, alterations in RNA steadystates in both the chloroplast and nuclear-cytosolic compartments are insignificant. We propose that the splicing and translation impairments are the underlying causes for the inability to produce normally green tissue in cp29a mutants under long-term cold conditions for the following reasons.

Firstly, most of the chloroplast genes containing introns are directly involved in the production of the photosynthetic apparatus or encode essential components of the chloroplast gene expression machinery (de Longevialle et al. 2010; Small et al. 2023). For example, the proteins encoded by intron-containing genes atpF and petB/ petD are vital components of the chloroplast ATP synthase and the cytochrome $b_6 f$ complex, respectively (Till et al. 2001; Kroeger et al. 2009). Knocking out any of these three genes results in the loss of photosynthesis, leading to pale tissue (Schwenkert et al. 2007) and the absence of splicing in atpF alone leads to pale plants and seedling death (Till et al. 2001). Therefore, a reduction in splicing efficiency for atpF and petB/petD is expected to strain the assembly of the photosynthetic machinery, which becomes critical in cold temperatures where photosystem assembly is expected to be slower.

In addition to the direct impact on photosynthesis gene expression, cold-treated cp29a mutants are expected to face general difficulties in producing the chloroplast gene expression machinery, particularly the ribosome. We identified three chloroplast mRNAs encoding ribosomal proteins L2, S12, L16 that show reduced splicing efficiency. Among them, rpl2 exhibits the most significant splicing defect in our dataset. Therefore, the most plausible explanation for the observed translation defect in cold-treated cp29a mutants is the reduced splicing deficiencies of these three mRNAs and thus a limitation in ribosome production. It is however important to acknowledge that we cannot rule out a more direct role of CP29A in chloroplast translation at this stage. The central question remains: How does the reduced translation contribute to the failure to generate green tissue in cold-treated cp29a mutants? Loss of the chloroplast ribosome is embryonic lethal in Arabidopsis (Zoschke and Bock 2018), and hypomorphic mutations in ribosomal protein genes result in the loss of photosynthesis (Bobik et al. 2019; Dupouy et al. 2022). Therefore, the general reduction in chloroplast translation in cold-treated cp29a mutants is expected to contribute to the inability to produce photosynthetic tissue. In bacteria, the production and maintenance of ribosomes themselves require specific proteins induced at low temperatures (Dammel and Noller 1995; Jones et al. 1996), and de novo assembly of newly synthesized bacterial ribosomes is stimulated during cold

shock (Charollais et al. 2004). Interestingly, many mutants affecting chloroplast translation exhibit bleaching phenotypes induced by low temperatures, suggesting that any impairment of chloroplast translation will compromise chloroplast development and thus the production of green tissue (Liu et al. 2010; Kusumi et al. 2011; Gao et al. 2022). In fact, a general decrease in translation caused by splicing defects in ribosomal protein mRNAs will also impact the production of chloroplast ribosomes themselves, amplifying the defect. Together, deficiencies in chloroplast translation likely contribute to, if not decisively cause, the failure of chloroplast development in cp29a mutants in cold conditions.

Nucleoids as neighbors of a chloroplast RNA processing compartment

Chloroplast DNA is structured into nucleoids, which consist of multiple chromosomes and associated proteins. Our study reveals that the droplets formed by CP29A are primarily found in close proximity to nucleoids. This observation bears similarity to the formation of RNA droplets in the mitochondria of metazoans, which are also spatially associated with nucleoids (Antonicka et al. 2013; Jourdain et al. 2016). The localization of CP29A droplets near nucleoids suggests a potential functional connection between these two cellular components. Just as RNA granules in mitochondria are believed to play a role in RNA regulation and processing, the proximity of CP29A granules to nucleoids implies a similar involvement in chloroplast RNA-related processes. Nucleoid-associated mitochondrial granules contain newly synthesized mitochondrial RNA and contain various RNA-binding proteins and RNases required for RNA maturation (Borowski et al. 2012; Pearce et al. 2017). Currently, the composition of CP29A-containing droplets remains unclear, and its protein interaction partners are unknown. Interestingly, a fraction enriched with nucleoids from maize contained factors involved in mRNA processing, splicing, and editing, including homologs of CP29A (Majeran et al. 2011). This led to the suggestion that RNA processing occurs co-transcriptionally. Our identification of a droplet structure adjacent to nucleoids suggests that further subcompartmentalization of gene expression takes place in chloroplasts, separate from nucleoids. The observed distance of 200 to 240 nm between nucleoids and CP29A droplets implies the possibility of an RNA bridge formed by nascent transcripts (considering that a 1,000-nucleotide (nt) RNA molecule is approximately 300 nm in length). This proximity suggests that nascent transcripts could directly interact with CP29A droplets, facilitating RNA processing and other related molecular events. While splicing may be one function of such granular structures, it remains an exciting question for future studies whether other RNA processing steps occur here or in additional separate compartments. The existence of PLDs in a large number of plant proteins suggests that we can anticipate the discovery of many more phase condensation events, including those occurring within organelles (Chakrabortee et al. 2016).

CP29A droplets as a compartment for cold acclimation

In metazoans, PS processes are used as temperature sensors in various contexts (Li and Fang 2020). Plants, as sessile organisms, need mechanisms to acclimate to changing temperatures. However, examples of temperature-dependent PS in plants are rare. In Arabidopsis, increased temperature leads to PLD-mediated PS of EARLY FLOWERING 3 (ELF3), which regulates the circadian clock (Jung et al. 2020). Another example is GUANYLATE BINDING PROTEIN LIKE 3 (GBPL3), which undergoes PS through a C-terminal IDR, resulting in the activation of target promoters

during pathogen infection—a process impaired at higher temperatures (Huang et al. 2021a). Similarly, higher temperatures lead to the dissolution of PS-dependent, phytochrome-containing photobodies, thereby modulating light-responsive gene expression (Chen et al. 2022). CP29A differs from these PS events in terms of its specific occurrence and importance at low temperatures. An analogous example for cold-induced PS in plants is how the FRIGIDA protein is sequestered in condensates to regulate vernalization (Zhu et al. 2021). CP29A's ability to autonomously and rapidly form condensates in response to lower temperatures in vitro and to occur in granular structures upon cold exposure in vivo together with its cold-specific function in chloroplast development make it a possible chloroplast cold sensor.

At first glance, CP29A droplets appear similar to cytosolic stress granules in mammals and yeast, which can be induced by low temperatures (Hofmann et al. 2012). However, stress granules mostly repress translation and may eventually contribute to RNA degradation (Hofmann et al. 2012). In contrast, CP29A droplets seem to support the accumulation of spliced transcripts and facilitate translation. We interpret CP29A as a factor that helps maintain the chloroplast gene expression program under lowtemperature conditions, while stress granules aid in terminating a gene expression program, paving the way for preparing an alternative program to counter the stress (Ivanov et al. 2019). It should be noted that the temperatures used to induce stress granules in mammals are considered well outside the regular physiological range that occurs in mammalian tissues (lowering from 37 to 10°C; Hofmann et al. 2012), while CP29A becomes relevant during mild temperature changes (21 to 12 °C) that frequently occur throughout the seasons in plant leaves. Thus, cold-dependent PS of CP29 occurs at relevant temperatures where the ability to sense and react to dropping temperatures is permanently needed.

Another interesting difference of CP29A PS compared to other thermo-sensitive PS events may lie in the mechanism of droplet formation. Several other RNA-binding proteins that exhibit temperature-dependent PS, such as Fused in Sarcoma (FUS), heterogeneous nuclear ribonucleoprotein A1 (hnRNPA1), or the poly(A)binding Protein1 (Pab1), utilize their RNA-binding domains next to their IDRs to drive PS (Burke et al. 2015; Molliex et al. 2015; Riback et al. 2017; Yoshizawa et al. 2018). For example, in the case of FUS, PS is supported by the cold denaturation of its zinc finger domain (Félix et al. 2023). Our in vitro and in vivo deletion analyses suggest that for CP29A, the PLD is the dominant factor in mediating cold-induced PS. We hypothesize that the RRMs remain intact and uninvolved during PS and fulfill important roles inside the droplet, likely in RNA binding. The fact that the PLD-less version of CP29A was still able to partially complement the macroscopic and splicing phenotype of the null mutant in the cold supports this idea. An alternative direct role of the PLD in splicing that is independent of phase-separation, for example by maintaining the required distance between the RRM domains necessary for RNA binding, remains a viable hypothesis. Identifying CP29A's RNA and protein partners within the droplet will be a crucial next step in understanding the exact mechanism of its effects on splicing and translation. CP29A has been identified in a proteome of heat-induced chloroplast stress granules together with other RNA binding proteins, including chloroplast RNA splicing and RNA editing factors (Chodasiewicz et al. 2020). These granules were induced by treating Arabidopsis seedlings for 30 min at 42 °C, conditions that led to irreversible aggregation of recombinant CP29A in our study. Targeted proteomic analyses are needed to show whether the cold-induced CP29A granules are related to these heat induced stress granules in protein composition and function.

The biochemical and biophysical conditions within chloroplasts with its light-induced changes in pH and redox state are in many aspects different from the nucleo-cytosolic compartment. Oxidative stress has been shown to induce stress granules in chloroplasts from the green algae Chlamydomonas reinhardtii, the only other case of a granule affecting gene expression in chloroplasts (Uniacke and Zerges 2008), cpRNPs are missing in green algae (Ruwe et al. 2011) and stress granules in C. reinhardtii are likely functionally and mechanistically quite different from CP29A droplets. CP29A homologs are common in land plants (Ruwe et al. 2011), yet their PLD varies substantially in both sequence and length (Supplementary Fig. S9). Interestingly, within subtaxa in dicotyledonous plants, some species have long PLDs while others in the same group exhibit short PLDs (Supplementary Fig. S9). The ability of CP29A variants, particularly those with shorter PLDs or differing amino acid compositions, to undergo PS and their role in cold resistance remains an open question. Our deletion analysis suggests that CP29A versions with shorter PLDs may not phase-separate as efficiently as the Arabidopsis protein. To further understand the specific sequence determinants, examining the diversity of Arabidopsis accessions could be a valuable initial step. This would help determine how PLD sequence variations affect PS and the protein's functionality in temperature-sensitive responses across various growth temperature ranges.

Materials and methods Bacterial strains and growth

DH5 α E. coli (Invitrogen-Thermo Fisher, Hennigsdorf, Germany) was used for vector amplification and passing, while BL21 E. coli (Invitrogen-Thermo Fisher, Hennigsdorf, Germany) was used for protein expression. E. coli cultures were grown at 37 °C under constant shaking (180 rpm) in standard lysogeny broth (LB) medium. Agrobacterium tumefaciens GC3103 cultures were grown at 28 °C under constant shaking (200 rpm) in standard LB medium.

Plant lines

Arabidopsis (Arabidopsis thaliana) null mutants of CP29A (cp29a-6) were obtained from the SALK Institute (San Diego) and were previously described (Kupsch et al. 2012). For transformation, the cp29a-6 line was grown under standard conditions (long day conditions; $120 \, \mu \text{E s}^{-1} \, \text{m}^{-2}$) in a growth chamber. Agrobacterium-mediated transformation was carried out using the standard floral dip

Antibody production

A section of the CP29A gene encoding the region from the 76th amino acid in exon 1 and to the 4th amino acid before the end of the reading frame was amplified from cDNA using oligonucleotides AG-cp29A+B_for and AG-cp29A+B_rev. The expressed and purified peptide was 264 amino acids long and was used for antibody production in rabbits (Pineda, Berlin, Germany).

Plant growth conditions

Arabidopsis seeds were stratified at 4 °C in the dark for 3 d and then grown at 21 °C with a light intensity of 120 $\mu mol~m^{-2}~s^{-1}$ (LED). For short-term cold treatment, plants were grown on soil for 14 d at 21 °C and then transferred to 12 or 8 °C for 3 or 10 d. To analyze the effects of long-term cold stress on cp29a and wt plants, both sets of plants needed to be at the same developmental stage. Due to slower growth under cold stress, cold-stressed plants were cultivated for 21 d to reach a comparable

developmental stage as unstressed plants grown for 10 d at 21 °C. This involved an initial cultivation at 21 °C for 5 d, followed by an additional 16 d at 8 °C. Before harvesting, cotyledons were removed since the phenotypic effect of CP29A knockout under cold conditions is primarily observed in newly formed tissues.

Construction of plant transformation vectors and plant transformation

Transformation vectors for the preparation of plant transgenic lines carrying meGFP and SNAP Tags were generated by HiFi assembly. The promoter region of CP29A (At3g53460) was amplified with the primer pair pcp29A+70aa_frw and pcp29A+SP70aa_rev, resulting in a 1,454 bp fragment (all oligonucleotides used for cloning can be found in Supplementary Table S4). A monomeric GFP fragment was obtained using the primer pair meGFP FL CP29A_frw and meGFP FL CP29A_rev, yielding a 722 bp fragment. The full-length genomic sequence of CP29A was amplified with the primer pair CP29A genomic+3UTR_frw and CP29A genomic+3UTR_rev, resulting in a 2,234 bp fragment. These three fragments were mixed in equimolar concentration with the pGL1 Vector cut with BamHI and HindIII. HiFi Assembly was performed following the manufacturer's protocol (NEB, Frankfurt, Germany), resulting in the generation of a vector named pGL1-CP29Apro:meGFP-CP29Afl.

For an analogous SNAP-tagged version of the full-length protein, the promoter region, SNAP Tag, and genomic fragment of CP29A were amplified with the following primer pairs: pcp29a+70aa_frw and pcp29A+70aa_rev for the promoter region, SNAptag_frw and SNAPtag_rev for the SNAP Tag, and CP29AFL SNAPtag_frw and CP29AFL SNAPTag_rev for the genomic fragment. The size of the SNAP Tag fragment was 579 bp, while the sizes of the other fragments were as described above for the GFP construct. After HiFi assembly into pGL1, the vector was named pGL1-CP29Apro:SNAP-CP29Afl.

To obtain a version of the constructs without the PLD domain, additional primer pairs were used. The promoter region and the GFP tag were amplified using the same primer pairs as before. A first genomic CP29A fragment, encompassing the RRM1 region, was amplified with the primer pair CP29Amidpart-PLD_frw and CP29Amidpart-PLD_rev, resulting in a 927 bp fragment. The second part of the genomic CP29A sequence, excluding the PLD domain, was amplified with the primer pair CP29ACterm-PLD_frw and CP29ACterm-PLD_rev, resulting in a 1230 bp fragment. After combining these PCR fragments with the pGL1 Vector, a HiFi assembly reaction was performed, resulting in the generation of a vector named pGL1-CP29Apro:meGFP-CP29AΔPLD.

After confirming the sequence of the PLD-less meGFP-tagged construct through Sanger sequencing, the primer pair for the fulllength SNAP Tag construct was used on the template of a GFP construct lacking the PLD domain. This allowed for the generation of a SNAP Tag version of the construct without the PLD domain, resulting in a PCR fragment of 2,139 bp. The resulting vector was named pGL1-CP29Apro:SNAP-CP29AΔPLD. Primer design was performed using NEBuilder v2.8.1 (https://nebuilder.neb.com/#!/).

Bacteria carrying all fragments in the pGL1 Vector derivatives were selected on LB media supplemented with Kanamycin. Transgenic plants generated by Agrobacterium-mediated transformation were selected on soil by spraying with BASTA. At least three independent lines per construct were isolated.

Photosynthetic measurements

In vivo chlorophyll a fluorescence was monitored with the Imaging PAM chlorophyll fluorimeter (Imaging PAM, M-Series; Walz, Effeltrich, Germany). Plants were dark-adapted for 15 min and measured according to standard protocols (Klughammer and Schreiber 2008).

Construction of bacterial expression vectors

Vectors for the expression of the CP29A protein in E. coli were prepared using the HiFi Assembly protocol with primer-based cloning. To amplify the full-length version of the CP29A protein, the primer pair Nitin_RRM1+2ext(wt)fw and Nitin_RRM1+2ext(wt)rev was used, resulting in a 837 bp fragment. This fragment was assembled into the pETM11 vector backbone, which had been cut with Ncol and BamHI, generating a vector named pETM11-CP29A FL.

Similar protocols were followed for the preparation of constructs for NMR measurements. For the construct carrying only the first RRM1 domain, the primer pair FR09 and FR10 was used, resulting in a 321 bp fragment. The fragment carrying the RRM2 domain was amplified using the primer pair FR11 and FR12, also resulting in a 321 bp fragment. Each of these fragments was inserted into the pETM11 vector, which had been cut with NcoI and BamHI, using HiFi Assembly. The vectors were named pETM11-RRM1 and pETM11-RRM2, respectively.

For cloning of the PLD-only domain, the primer pair Nitin_ PLD_fw and Nitin_PLD_rev was used, resulting in a fragment of an unspecified size. This fragment was cloned into the pTrx Vector backbone, which had been cut with NcoI and BamHI, and processed with the HiFi Assembly Kit (NEB, Frankfurt, Germany). The resulting vector was named pTrx-CP29APLD core.

For droplet formation assays, constructs were prepared in the pETM11 vector backbone. These constructs contained the mNeonGreen Tag fused to the N-terminal side of the CP29A protein. The CP29A full-length version was amplified using the primer pair pETM11 mNeonGreen frw and mNeonGreen29Arev which resulted in a PCR fragment size of 956 bp. The mNeonGreen Tag was amplified separately using the primer pair mNeonGreen29A_frw and pETM11 29A_rev which resulted in the fragment size of 753 bp. The combination of these PCR products with the NcoI and BamHI-digested pETM11 vector produced the pETM11-mNG: CP29AFL expression vector.

The PLD domain fused to the mNeonGreen Tag was amplified using the primer pairs pETM11-mNeonGreen_frw and mNeon Green_PLD_cor_rev and the PCR product obtained was of 753 bp in size, as well as mNeonGreen PLD_cor_frw and pETM11_ PLD_cor_rev which amplified a PCR product of 264 bp in size. The resulting fragments were used for HiFi assembly to generate the pETM11-mNG:PLDcore vector.

Protoplast isolation and microscopy

For protoplast isolation, plants were grown on soil for 14 d at standard growth conditions and used for protoplast isolation (Yoo et al. 2007). 10⁶ protoplasts were used for in vivo labeling. SNAP-tagged proteins were labeled with Cell-SiR647 (NEB, Frankfurt, Germany). Labeling was done at room temperature (RT) for 1 h, according to the manufacturer's protocol. After labeling, a wash step with MMG Buffer was included before fixation. Protoplasts were fixed in ice cold 4% (w/v) paraformaldehyde in the PBS buffer pH7.2 for 15 min. After fixation, three wash steps with ice cold methanol were used for chlorophyll extraction. After a PBS wash, DAPI staining (50 ng/mL) was done in PBS buffer at RT for 30 min. The DAPI stain was washed off five times with PBS Buffer. Slides with fixed protoplasts were analyzed using different microscopes. An Abberior Facility Line Confocal Microscope (Abberior GmbH, Göttingen, Germany) was used to produce the image shown in Fig. 3A. For Fig. 3B, protoplasts were mounted in Prolong Mountant (Invitrogen, Hennigsdorf, Germany) for STED Microscopy on a Leica TCS SP8 3X (Leica, Wetzlar, Germany). A deconvoluted image of the STED scan is shown, performed with Leica Las X & Huygens Deconvolution software. For Fig. 3E, protoplasts were mounted in Mowiol (Fang et al. 2019) for STED and confocal imaging using the STED Abberior Facility Line machine (Abberior, Göttingen, Germany) and a 100x oil-immersion objective. The DAPI signal of nucleoids was excited with a 405 nm laser, and the emitted light was collected with a detector in the range of 415 to 525 nm. The SNAP Cell SiR647 dye was excited with a 640 nm laser in confocal or STED mode, and the emitted light was collected within the range of 650 to 735 nm for autofluorescence of chlorophyll and fluorescence of SiR647, respectively. SNAP dye-labeled droplets were detected by STED microscopy using excitation at 640 nm and a detecting spectrum of 650 to 735 nm, while the STED laser emitting light used here was at 775 nm with a gate of 750 ps (+8 ns). Figure 3G shows confocal images from live cell imaging of plant tissue grown at room temperature and plants exposed to cold conditions for 3 d at 12 °C. Simultaneous images were taken in the meGFP and STAR635 channels in order to detect meGFP and chlorophyll autofluorescence. Excitation of meGFP was performed with a laser at 518 nm, and the emitted light was collected in the range of 520 to 550 nm, while the STAR635 signal was excited with a laser at 640 nm, and the emitted light was collected within the range of 645 to 670 nm.

Immunofluorescence assay of CP29A droplets in protoplasts

 2×10^6 protoplasts were allowed to adhere for 10 min at room temperature on poly-L-lysine-coated slides. The protoplasts were then fixed with 4% (w/v) formaldehyde in PBS (137 mm NaCl, 2.7 mm KCl, 10 mm Na_2HPO_4, 2 mm KH_2PO_4) for 20 min at room temperature. To extract chlorophyll, the cells were incubated for 2×10 min at -20 °C in precooled methanol. Afterwards, the fixed cells were washed for 2×10 min in PBS-Mg (5 mm MgCl $_2$ in PBS). Permeabilization was carried out at room temperature for 10 min in 2% (v/v) Triton or 4% (v/v) DMSO in PBS. The protoplasts were then equilibrated for 2×10 min in PBS-Mg and subsequently used for immunofluorescence staining.

The fixed protoplasts were blocked for 30 min at room temperature in 0.5% (v/v) BSA in PBS, pH 7.2. The cells were incubated for 75 min at 37 °C with 2% (v/v) Triton in PBS for 10 min at RT to improve penetration of the antibody. The cells were then incubated with the primary antibody against CP29A (Kupsch et al. 2012; diluted in 0.5% BSA (v/v) in PBS; dilutions of 1:50 or 1:500 were used). After washing twice for 10 min in PBS-Mg, the cells were incubated with a fluorescein-labeled secondary antibody (Merck, Darmstadt, Germany; diluted in 0.5% (v/v) BSA in PBS) for 45 min at room temperature in the dark. The samples were then equilibrated again for 2 × 10 min in PBS-Mg. Finally, a drop of the permanent mountant VECTASHIELD HardSetTM Antifade Mounting Medium (Life Technologies, Carlsbad) was added to cover the cells. To preserve the preparation, the specimen was sealed with nail polish.

Epifluorescence microscopy of immunofluorescence assays were carried out with a IX71 Δ Vision Spectris Restorations microscopy system (Olympus, Tokyo), employing the 100x Plan Apo objective (numerical aperture 1.4).

Protein expression and purification

mNG-CP29AFL, mNG-CP29A Δ PLD, and mNG-PLD were expressed in E. coli BL21 at 18 °C overnight after induction with 0.1 mm

isopropyl β-D-1-thiogalactopyranoside. Bacterial pellets were resuspended in a resuspension buffer (20 mm Na-Phosphate Buffer pH 7.4, 300 mm NaCl and 1 mg/mL Lysozyme). Cells were lysed by sonication and the lysate was centrifuged at $12,000 \times g$ for 15 min at 4 °C. Supernatants were incubated with prewashed agarose Ni-NTA beads (Cytiva, Freiburg). Bound protein was washed five times with five volumes of the bead bed with increasing NaCl concentration (Wash Buffer 1: 10 mm Tris pH8, 300 mm NaCl+5 mm imidazole; Wash Buffer 2: 10 mм Tris pH8, 500 mм NaCl + 5 mм imidazole; Wash Buffer 3: 10 mm Tris pH8, 1000 mm NaCl; Wash Buffer 4: 10 mm Tris pH8, 1500 mm NaCl). Before elution, a TEV cleavage step was performed with addition of 1,000 U of the enzyme per mL of the suspension. Elution of the bound protein was done in three volumes of the bead bed (150 mm NaCl, 10 mm Tris pH 8, 300 mm imidazole, 1 mm DTT, 0.5 mm EDTA). Eluate was concentrated using centricon tubes (Merck, Darmstadt). Protein concentrations were estimated via Bradford assays using a BSA standard. Protein purity was estimated via PAGE-SDS and subsequent CBB staining of the gel.

In vitro phase separation assays

In vitro PS assays with purified recombinant protein were performed in low salt buffer (10 mm Tris pH 8.0, 50 mm NaCl, 1 mm DTT, 0.5 mm EDTA, 2.5% (v/v) Glycerol) with 50 μm protein unless otherwise indicated. Crowding agent was added to 10% as a final concentration through mixing with the microscopy solution (20% (w/v) PEG 8,000 in low salt buffer). After mixing, the sample was applied to an 8-well glass-bottom slide (Ibidi, Gräfelfing, Germany), incubated at room temperature for 30 s before being imaged on an Abberior Facility line Microscope with Light Box software using 100x oil magnification objective. Droplet formation was followed over time by collecting a series of images using a 488 nm excitation laser (3% power). All droplet assays were repeated at least three times. For cold treatment, the protein solution was incubated on ice for 10 min prior to microscopy.

For co-condensation assays with total plant RNA, mNG-CP29A, RNA and 10% (w/v) PEG (FC) were mixed, incubated at 21 $^{\circ}$ C for 5 min and then directly imaged. For each concentration, four images were taken in the four corners of the solution in the microscopy well and two additional images in the center of the well. For co-condensation with specific chloroplast transcripts, 2 ng of in vitro transcribed RNA was used.

To investigate the temperature dependence of droplet formation, a 50 $\mu \rm M$ protein solution was combined with PEG 8,000 to achieve a final concentration of 10% (w/v). This mixture was incubated for 5 min at either 21 or 4 °C. Post-incubation, the sample was examined using a microscope equipped with a 100× oil immersion objective. A visual plane above the glass bottom was selected to prevent the scoring of droplets adhering to the glass surface. Subsequently, an automated scan covering a 300× 300 $\mu \rm m^2$ area was performed by the microscope to eliminate user-induced selection bias.

Quantifications of droplet size were done with a custom python script in ImageJ. After smoothing and background subtraction using a rolling ball algorithm, droplets were detected with the "Analyze Particles" plugin. The measured Feret's diameter—maximum diameter of a round object—was then plotted using R-Studio for different conditions.

Fluorescence recovery after photobleaching

For FRAP recordings, droplets observed in vitro were excited with a 488 nm laser line on a confocal Abberior Facility line microscope

by using a 100x oil objective. A region of interest was selected within the condensate and 100% power of STED laser was used for bleaching. Five images were taken prior to bleaching and postbleaching recovery of fluorescence was recorded for up to 55 s at a frame interval of 1 s. Evaluation of the FRAP analysis was done with ImageJ and custom written Python scripts. In brief, for each condition at least 11 trajectories were analyzed. First, trajectories were normalized to intensity values before photobleaching and then averaged, the standard deviation is represented as shadow for each condition in Fig. 1F. Next, fluorescence intensity recovery trajectories were offset to the first intensity value Ioff after the photobleaching event and fitted using custom written Python scripts with the formula:

$$I(t) = A \cdot (1 - \exp(-t^*\tau)).$$

Here A (+ Ioff as described in the corresponding python script) corresponds to the plateau intensity representing the mobile fraction of proteins, τ is the recovery time and t is the time after the bleach pulse. Imaging and bleaching conditions, such as laser intensity and time were strictly kept constant in between conditions to compare mobile fraction and recovery half time (Carnell et al. 2015; McSwiggen et al. 2019). Bleaching of area to total area of the droplet was not compensated as the model assumes protein recovery from the solution. From the fit τ is extracted to calculate the recovery half time $t\frac{1}{2}$:

$$t1/2 = \ln(2)/\tau$$

Distance measurements between CP29A droplets and nucleoids

The shortest distance for every CP29A droplet was measured to its closest nucleoid based on STED microscopy images with an approximate resolution of 60 nm using an Abberior instrument. ImageJ was then used to perform peak detection in both channels. A custom written python script was further used to calculate minimal distances between CP29A and nucleoid pairs. The minimal distances were plotted as a histogram and fitted with a kernel density estimation. At least five field of views containing a minimum of 20 chloroplasts each were analyzed per condition. To confirm the performance of this experiment, we calculated the number of CP29A droplets and nucleoids per chloroplast volume and used a custom written python script to randomly position them. The same script was then used to measure distances. A normalized probability density function to estimate the average distance between centers resulted in a mean of 0.46 μ m.

NMR spectroscopy

N-terminal His₆-tagged RRM1 (97 to 176 aa), RRM2 (255 to 334 aa), RRM1,2 (97 to 334 aa) and His6-thioredoxin tagged PLD (176 to 254 aa) constructs were over-expressed in E. coli BL21 (DE3) in M9 minimal media supplemented with ¹⁵N NH₄Cl and/or ¹³C glucose as the sole nitrogen and carbon sources, respectively. Cells were harvested, lysed using a French press, and the respective proteins were purified by affinity chromatography with Ni-NTA sepharose followed by TEV cleavage as mentioned above. Further purification steps were carried out by ion-exchange and size-exclusion chromatography. The final buffer for NMR samples contained 20 mm sodium phosphate (pH 6.8), 50 mm NaCl, 1 mm DTT. The sample quality was checked by SDS-PAGE and ESI-mass spectrometry.

Backbone and side-chain chemical shifts for RRM1, PLD, and RRM2 constructs of CP29A were assigned from conventional 3D NMR experiments, such as HNCACB, CBCA(CO)NH, HNCO, HN(CA)CO, HNN, (H)CCCONH, H(CCCO)NH, and 15N-edited NOESY-HSOC (Sattler 1999; Panchal et al. 2001). NMR measurements were performed on Bruker spectrometers with a proton Larmor frequency of 500, 600, 800, 900, 950 or 1,200 MHz equipped with cryogenic or room temperature ¹H, ¹³C and ¹⁵N triple resonance probe detection. 5% (v/v) D₂O was added to the samples to lock the external magnetic field, NMR samples were put into 3, 5 mm or Shigemi tubes. ¹H, ¹⁵N HSQC spectra were acquired with 100 and 60 ms acquisition time in direct and indirect dimensions, respectively. Spectra were processed with Bruker Topspin 3.5pl6 or NMRPipe (Delaglio et al. 1995) with a shifted sine-bell window function and zero filling before Fourier transformation. Proton chemical shifts were referenced against sodium 2,2-dimethyl-2-silapentane 5-sulfonate (DSS). Spectra were analyzed using the CCPN (v2.5) software tool (Vranken et al. 2005). Steady-state {1H-}-15N heteronuclear NOE experiments (Farrow et al. 1994) were recorded with 170 and 168 ms acquisition times in the direct and indirect dimension, respectively with 3 s recycle delay and 32 scans. Spectra were split with a Bruker AU program, further processed in Topspin and then analyzed using CCPN.

Secondary structural elements for RRM1, PLD, and RRM2 domains were derived from NMR backbone and side-chain chemical shifts using TALOS-N and compared with an AlphaFold2 model. The structural model of RRM1-PLD-RRM2 was generated using CNS (v1.2; Shen and Bax 2013) by keeping the ternary fold of both RRMs (obtained from AlphaFold2), while the coordinates for the PLD linker were randomized. The electrostatic surface charges for CP29a were calculated using the APBS tool (Baker et al. 2001).

Small-angle X-ray scattering measurements

SAXS experiments were carried out in-house on a Rigaku BIOSAXS1000 instrument comprising a Rigaku HF007 microfocus rotational anode with a copper target (40 kV, 30 mA). Transmissions were measured with a photodiode beam stop and calibration was done with a silver behenate sample (Alpha Aeser). All samples were dialyzed overnight with SAXS buffer (20 mm sodium-phosphate, pH 6.5, 30 mm NaCl) before the measurements. Samples with concentrations from 4 to 16 mg/mL were measured at 25 and 4 °C temperature to assess concentration dependent effects. Multiple buffer samples were measured in between each run and buffer subtraction was applied using the SAXSLab software. Further data analysis was done using the ATSAS package (v3.0.5; Manalastas-Cantos et al. 2021).

Immunoblots

Equal amounts of total leaf protein were separated on an SDS-PAGE gel and blotted onto a nitrocellulose membrane (Cytiva, Freiburg, Germany). Membranes were blocked in 4% milk (w/v) TBST solution for 1 h, washed twice with TBST solution and incubated with a CP29A/B-specific rabbit antisera (Kupsch et al. 2012) or anti-SNAP rabbit antisera (NEB, P9310, Frankfurt, Germany) or antiplant-actin antibody (antibodies.com, A17309, Stockholm, Sweden) in 1:2,000 dilution overnight at 4 °C and subsequently washed with TBST buffer four times at room temperature. Secondary antibodies (either antimouse IgG (Abcam, ab205720, Cambridge, UK) or antirabbit IgG (Abcam, ab205718, Cambridge, UK), both conjugated to HRP) were used at a dilution of 1:10,000 for GFP/CP29A primary antisera or at 1:5,000 for the SNAP primary antisera and incubated for 1 h at room temperature. Four washes with TBST buffer were done prior to chemiluminescence detection.

RNA isolation and library construction for RNA-seq

Plant tissue was frozen in liquid nitrogen and pulverized in a mortar. Total RNA was isolated by acid guanidinium thiocyanate–phenol–chloroform-based extraction and purified from the aqueous phase using the Monarch RNA Clean Up Kit (NEB, Frankfurt, Germany). RNA quality was assessed by agarose gel electrophoresis. Total RNA was sequenced on an Illumina platform using Novogene's (London) lncRNA-seq protocol, based on rRNA-depletion followed by strand-specific library construction. All libraries were sequenced with 150 bp paired-end reads.

RNA-seq-gene expression analysis

The nf-core/rnaseq (v3.10.1) pipeline was used for quality control, read processing, and mapping of the RNA-seq libraries. Hisat2 was used as an aligner and TAIR10 and Araport11 were provided to the pipeline as reference genome and annotation, respectively. FeatureCounts (Rsubread, 2.12.0) was used for read counting and DeSeq2 was used for DEG analysis after low read filtering (CPM>1 in all samples).

RNA-seq—splicing analysis

Splicing efficiencies were analyzed using the ChloroSeq pipeline, as described previously (Castandet et al. 2016). Fisher's exact test in combination with Benjamini–Hochberg correction was used for statistical testing.

RT-qPCR

For RT-qPCR analysis, genomic DNA in total RNA samples was removed using TURBO DNase (Thermo Fisher Scientific) followed by purification with the Monarch RNA Clean Up Kit (NEB, Frankfurt, Germany). gDNA removal was assessed by PCR on chloroplast DNA followed by agarose gel electrophoresis. RNA was transcribed to cDNA using the ProtoscriptII reverse transcriptase (NEB, Frankfurt, Germany). Luna qPCR Mastermix (NEB, Frankfurt, Germany) was used for amplification on an 7,500 Fast Real-Time PCR System (Applied Biosystems).

Preparation of labeled in vitro transcripts

PCR products for *psbA* or *rm23* were generated with primer pairs psbA.rp/psbA.T7 and rm23.T7/rm23.rp, respectively (psbA: 380 bp; rm23: 300 bp). Five hundred nanogram of purified PCR product was used as a template for in vitro transcription assay with azido UTP (Jena Bioscience, Jena, Germany, final conc. 10 mm). One microgram of the in vitro transcript was used for chemical labeling of the RNA with cy5.5 alkalyne label (Lumiprobe, Hunt Valley, USA, final con. 10 mm) for 2 h at 37 °C. Excess dye was removed by RNA clean and concentrator columns by following the manufacturer's protocol (NEB, Frankfurt, Germany).

Ribosome profiling

Isolation of ribosome footprints and total RNA

Wt Col-0 and cp29a-6 plants were grown at 21 °C in a 16/8 h light/dark regime for 15 d and after this were transferred to cold conditions, 12 °C, in a 16/8 h light/dark regime for 3 d. Three hundred and fifty microgram of frozen plant tissue was homogenized in liquid nitrogen with a mortar and pestle followed by the addition of 3.5 mL ribosome extraction buffer (0.2 $\,\mathrm{M}$ sucrose, 0.2 $\,\mathrm{M}$ KCl, 40 mM Tris-OAc pH 8.0, 10 mM MgCl₂, 10 mM 2-mercaptoethanol, 2% (v/v) polyoxyethylene (10) tridecyl ether, 1% (v/v) Triton X-100,

100 μg/mL chloramphenicol, 100 μg/mL cycloheximide). After brief mixing, a 0.5 mL aliquot of the lysate was flash frozen and stored at -80 °C for later total RNA extraction using TRIzol reagent (ThermoFisher cat# 15596026). The remaining lysate was filtered through glass wool, followed by centrifugation for 10 min at 15,000 × q at 4 °C to remove cell debris. Three milliliter of the clarified lysate were incubated with 1800U of RNase I (Ambion cat# AM2294) for 1 h at room temperature with gentle rotation. The ribonuclease-treated lysate contains mainly monosomes which were loaded onto a 2 mL sucrose cushion (30% (w/v) sucrose, 40 mm Tris-acetate pH 8.0, 100 mm KCl, 15 mm MgCl₂, 0.1 mg/mL chloramphenicol, 0.1 mg/mL cycloheximide, 0.2% (v/v) β-MeEtOH) and centrifuged (Optima L-80 XP Ultracentrifuge—Beckman Coulter) for 1.5 h at 303,800 \times g at 4 °C. The supernatant was then aspirated and the pelleted monosomes resuspended in 0.5 mL footprint isolation buffer (10 mm Tris pH 8.0, 1 mm EDTA pH 8.0, 100 mm NaCl, 1% (w/v) SDS, 0.1 m EGTA pH 8.0). The ribosome footprints were extracted from this pellet using 0.5 mL TRIzol reagent.

Next, ribosome footprints were size-selected through electrophoresis on a 12% (v/v) denaturing polyacrylamide gel (19:1, acrylamide:bisacrylamide) prepared in 1x TBE buffer (89 mm Tris, 89 mm boric acid, 2 mм EDTA pH 8.0) containing 8 м urea. To this end, approximately 60 μ g ribosome footprints were resuspended in 100 μ L of ribosome footprint loading buffer (90% (v/v) deionized formamide, 20 mm Tris-HCl pH 7.5, 20 mm EDTA pH 8.0, 0.04% (w/v) bromophenol blue, and 0.04% (w/v) xylene cyanol) and denatured for 10 min at 70 °C. The gel was run in 1x TBE buffer with a constant power of 30 W at constant temperature of 12 °C (achieved by a cooling unit). Co-migrating prestained RNA ladder (Biodynamics Laboratory cat# DM253) was used to visualize the regions of the gel to excise ribosome footprints (20 to 40 nt). Ribosome footprints were eluted from the excised gel piece in 16 mL TESS (10 mm Tris рН 8.0, 1 mм EDTA pH 8.0, 0.1 м NaCl, 0.2% (w/v) SDS) by overnight incubation at 4 °C with gentle rotation. Eluted ribosome footprints were isolated with 16 mL of phenol:chloroform:isoamyl alcohol (25:24:1), followed by overnight ethanol precipitation at -20 °C. To increase purity and further narrow the volume, the ribosome footprint pellet was resuspended in $0.1 \,\mathrm{M}$ NaCl (500 $\mu\mathrm{L}$) and subjected to a second round of phenol:chloroform:isoamyl alcohol (25:24:1) extraction, followed by two washes with chloroform:isoamylalcohol (24:1) and overnight ethanol precipitation at -20 °C. The received ribosome footprint pellet was washed twice with 75% (v/v) ethanol and resuspended in RNase-free water.

rRNA depletion of ribosome footprints

Oligo hybridization was performed following an adapted protocol from (Kraus et al. 2019). Gel-purified ribosome footprints (150 ng) were mixed with the following components in a PCR tube: $4 \mu L$ deionized formamide, 1 µL 20X SSC (3 м NaCl, 0.3 м Na-Citrate, pH 7.0 with HCl), $2 \mu L$ EDTA (5 mm, pH 8.0), $0.7 \mu L$ biotinylated oligo mix (100 µM, see Supplementary Table S5), and RNase free water up to 20 μ L. Hybridization of the oligos was performed in a thermocycler with heated lid using a slow temperature ramp with a ramp rate of 0.1 °C/s (ramp steps: 80 °C—5 min; 75 to 2 min; 70 to 2 min; 65 to 2 min; 60 to 2 min; 55 to 2 min; 50 to 2 min; 45 to 2 min; 40 to 2 min; 35 to 2 min). After oligo hybridization, each sample was topped off to 40 µL using a solution of 1X SCC and 20% (v/v) formamide and kept at 35 °C until ready for oligo removal, which was performed using Dynabeads MyOne C1 (Thermo Fisher cat# 65002). For each sample, 45 µL of beads were washed according to the manufacturer's protocol for RNA applications, and divided into 30 and 15 µL aliquots for performing two rounds of oligo

removal. Each sample was incubated with the 30 µL bead aliquot at room temperature for 15 min, and magnetized for 2 min. The second round of oligo removal was performed by aspirating the supernatant into the 15 μ L bead aliquot and repeating the incubation and magnetization. The final supernatant contains the rRNA-depleted ribosome footprints, which were aspirated, transferred into a clean tube and ethanol precipitated overnight at -20 °C. The rRNA-depleted ribosome footprint pellet was resuspended in RNase-free water and treated with TURBO DNase (Thermo cat# AM2238) according to the manufacturer's instructions, in order to remove traces of leftover DNA oligos. Following DNase treatment, ribosome footprints were purified using the Monarch RNA cleanup kit (NEB cat# T2030) following the modified protocol for small RNA.

Ribo-seq and RNA-seq library construction

To prepare the terminal ends for adapter ligation, rRNA-depleted ribosome footprints were treated with T4 polynucleotide kinase (PNK; ThermoFisher, cat#EK0031). The end-repaired ribosome footprints were purified using the Monarch RNA cleanup kit using the modified protocol for small RNA. These purified ribosome footprints were used as input for the NEXTflex small RNA-seq kit v3 (Perkin Elmer, cat# NOVA-5132-06). The resulting cDNA was amplified by 11 to 16 cycles of PCR with a barcode incorporated in the primer, and purified according to the instructions of the NEXTflex kit. For RNA-seq, 10 µg of purified total RNAs as described above were subjected to DNase treatment (TURBO DNase, Thermo cat# AM2238) following the manufacturer's instructions. The concentration of purified total RNA was quantified using a Qubit HS RNA assay (Thermo Fisher Scientific; Q32852). Then, 500 ng of purified total RNA was used to construct sequencing libraries using the Zymo-Seq RiboFree total RNA library kit (Zymo cat# R3000/R3003), which contains a step of an enzymatic degradation of rRNAs. Libraries were pooled for single-end 100-bp sequencing in a NovaSeq 6,000 machine.

Bioinformatic analysis was done using the RiboDoc pipeline (François et al. 2021), which features the riboWaltz package (Lauria et al. 2018) for P-site estimation and quality controls.

Statistical analysis

Statistical analyses were performed as described in each figure legend. Statistical data are provided in Supplementary Data Set S1.

Accession numbers

All RNA-seq and Ribo-seq data are available at SRA, bioproject accession PRJNA981550. Reviewer link prior to publication: https:// dataview.ncbi.nlm.nih.gov/object/PRJNA981550? reviewer=1crku8 tl9crm8itiiqd3sl742b.

NMR data are deposited at BMRB with the ID 52022 and 52025. SAXS data were deposited at SASBDB with the accession codes SASDT92 and SASDTA2.

Acknowledgments

We are grateful to I. Passow (HU Berlin) for assistance propagating Arabidopsis and F Reiher (HU Berlin) for support with in vitro PS experiments. We acknowledge NMR measurements at the Bavarian NMR Center (BNMRZ) at the Technical University of Munich, Germany. We thank Sam Asami, Gerd Gemmecker and Matthias Brandl for technical support with the NMR facility, and Ralf Stehle for his assistance with in-house SAXS measurements.

We acknowledge SBGrid and the NMRbox server for providing access to NMR software. We are also thankful to Dr. Gero Schlötel from Aberrior Microscope Facility as well as Dr. Karl-Heinz Körtje from Leica Microsystems for their initial support of the STED microscopy.

Author contributions

C.S. and M.S. conceived the study, designed the strategy, and supervised the experiments. J.L., B.L., N.K., S.G., and Y.G. performed the experiments and interpreted the data. S.M., W.W., E.K., and R.Z. analyzed datasets and interpreted data. C.S. wrote the manuscript, which was edited by all co-authors.

Supplementary data

The following materials are available in the online version of this article

Supplementary Figure S1. Sequence, structure, and PS analysis of recombinant CP29A.

Supplementary Figure S2. Small-angle X-ray scattering analysis of the PLD linker of CP29A.

Supplementary Figure S3. Phenotypic recovery of cp29a mutants after cold-induced bleaching of the center of the rosette.

Supplementary Figure S4. Accumulation of CP29A variants in transgenic Arabidopsis lines.

Supplementary Figure S5. Immunofluorescence analysis of CP29A during cold acclimation and FRAP attempts.

Supplementary Figure S6. Principal component analysis and retrograde signaling defects revealed by RNA-seq analysis of longterm cold-treated cp29a mutants.

Supplementary Figure S7. RNA-seq analysis of cp29a complementation lines after 3 and 10 d in the cold.

Supplementary Figure S8. Quality check of ribosome profiling data of short-term cold-treated plants.

Supplementary Figure S9. Alignment of the PLD domain in CP29A proteins across various relatives of A. thaliana.

Supplementary Table S1. FRAP data.

Supplementary Table S2. SAXS analysis of the PLD at different temperatures.

Supplementary Table S3. RNA sequencing reads for RNA-seq and Ribo-seq experiments of short-term treated wt and cp29a mutant plants.

Supplementary Table S4. Oligonucleotides used for cloning. Supplementary Table S5. Custom biotinylated DNA oligos for rRNA removal from Arabidopsis ribosome footprint samples.

Supplementary Data Set 1. Details on statistical analyses of splicing and Ribo-seq.

Video S1. Full-length CP29A in NMR buffer (120 μm protein; 20 mm sodium phosphate (pH 6.8), 50 mm NaCl, 1 mm DTT; see Fig. 1B for recombinant protein analysis) in cold water (4 °C, left test tube) and was returned to room temperature (25 °C; right test tube).

Video S2. Droplet formation and droplet fusion of mNG-CP29A in vitro

Funding

This research was supported by the German Research Foundation $\,$ via TR175-A02 to C.S., SPP1935 and SPP2191 to C.S. and M.S., and GRK1721, SFB1035 to M.S.

Conflict of interest statement. None declared.

Data and code availability

All data were analyzed using RStudio and Excel. Statistical tests, P values, number of biological and technical replicates, and number of independent experiments are indicated in the figure legends or main text and detailed results are provided in Supplementary Data Set S1. Scripts for FRAP analysis and analysis of droplet size are available here: https://github.com/klotzsch-lab/In-Vitro-Protein-Analysis/.

References

- Alberti S, Hyman AA. Biomolecular condensates at the nexus of cellular stress, protein aggregation disease and ageing. *Nat Rev Mol Cell Biol.* 2021:22(3):196–213. https://doi.org/10.1038/s41580-020-00326-6
- Antonicka H, Sasarman F, Nishimura T, Paupe V, Shoubridge EA. The mitochondrial RNA-binding protein GRSF1 localizes to RNA granules and is required for posttranscriptional mitochondrial gene expression. *Cell Metab.* 2013:17(3):386–398. https://doi.org/10.1016/j.cmet.2013.02.006
- Antonicka H, Shoubridge EA. Mitochondrial RNA granules are centers for posttranscriptional RNA processing and ribosome biogenesis. *Cell Rep.* 2015:10(6):920–932. https://doi.org/10.1016/j.celrep. 2015.01.030
- Baker NA, Sept D, Joseph S, Holst MJ, McCammon JA. Electrostatics of nanosystems: application to microtubules and the ribosome. *Proc Natl Acad Sci U S A.* 2001:98(18):10037–10041. https://doi.org/10.1073/pnas.181342398
- Bobik K, Fernandez JC, Hardin SR, Ernest B, Ganusova EE, Staton ME, Burch-Smith TM. The essential chloroplast ribosomal protein uL15c interacts with the chloroplast RNA helicase ISE2 and affects intercellular trafficking through plasmodesmata. New Phytol. 2019:221(2):850–865. https://doi.org/10.1111/nph.15427
- Boke E, Ruer M, Wühr M, Coughlin M, Lemaitre R, Gygi SP, Alberti S, Drechsel D, Hyman AA, Mitchison TJ. Amyloid-like self-assembly of a cellular compartment. *Cell.* 2016:166(3):637–650. https://doi.org/10.1016/j.cell.2016.06.051
- Borowski LS, Dziembowski A, Hejnowicz MS, Stepien PP, Szczesny RJ. Human mitochondrial RNA decay mediated by PNPase–hSuv3 complex takes place in distinct foci. Nucleic Acids Res. 2012:41(2): 1223–1240. https://doi.org/10.1093/nar/gks1130
- Bose M, Lampe M, Mahamid J, Ephrussi A. Liquid-to-solid phase transition of oskar ribonucleoprotein granules is essential for their function in Drosophila embryonic development. *Cell.* 2022:185(8): 1308–1324.e23. https://doi.org/10.1016/j.cell.2022.02.022
- Burke KA, Janke AM, Rhine CL, Fawzi NL. Residue-by-residue view of in vitro FUS granules that bind the C-terminal domain of RNA polymerase II. Mol. Cell. 2015:60(2):231–241. https://doi.org/10. 1016/j.molcel.2015.09.006
- Carnell M, Macmillan A, Whan R. Fluorescence recovery after photobleaching (FRAP): acquisition, analysis, and applications. *Methods* Mol Biol. 2015:1232:255–271. https://doi.org/10.1007/978-1-4939-1752-5 18
- Castandet B, Hotto AM, Strickler SR, Stem DB. ChloroSeq, an optimized chloroplast RNA-Seq bioinformatic pipeline, reveals remodeling of the organellar transcriptome under heat stress. G3 (Bethesda). 2016;6(9):2817–2827. https://doi.org/10.1534/g3.116.030783
- Chakrabortee S, Kayatekin C, Newby GA, Mendillo ML, Lancaster A, Lindquist S. Luminidependens (LD) is an Arabidopsis protein with prion behavior. *Proc Natl Acad Sci U S A.* 2016:113(21): 6065–6070. https://doi.org/10.1073/pnas.1604478113
- Charollais J, Dreyfus M, Iost I. CsdA, a cold-shock RNA helicase from Escherichia coli, is involved in the biogenesis of 50S ribosomal

- subunit. Nucleic Acids Res. 2004:32(9):2751–2759. https://doi.org/10.1093/nar/gkh603
- Chen D, Lyu M, Kou X, Li J, Yang Z, Gao L, Li Y, Fan L-M, Shi H, Zhong S. Integration of light and temperature sensing by liquid-liquid phase separation of phytochrome B. Mol Cell. 2022:82(16): 3015–3029.e6. https://doi.org/10.1016/j.molcel.2022.05.026
- Chodasiewicz M, Sokolowska EM, Nelson-Dittrich AC, Masiuk A, Beltran JCM, Nelson ADL, Skirycz A. Identification and characterization of the heat-induced plastidial stress granules reveal new insight into arabidopsis stress response. Front Plant Sci. 2020:11: 595792. https://doi.org/10.3389/fpls.2020.595792
- Chotewutmontri P, Barkan A. Dynamics of chloroplast translation during chloroplast differentiation in maize. PLoS Genet. 2016:12(7): e1006106. https://doi.org/10.1371/journal.pgen.1006106
- Dammel CS, Noller HF. Suppression of a cold-sensitive mutation in 16S rRNA by overexpression of a novel ribosome-binding factor, RbfA. *Genes Dev.* 1995:9(5):626–637. https://doi.org/10.1101/gad. 9.5.626
- Delaglio F, Grzesiek S, Vuister GW, Zhu G, Pfeifer J, Bax A. NMRPipe: a multidimensional spectral processing system based on UNIX pipes. J Biomol NMR. 1995:6(3):277–293. https://doi.org/10.1007/BF00197809
- de Longevialle AF, Small ID, Lurin C. Nuclearly encoded splicing factors implicated in RNA splicing in higher plant organelles. Mol Plant. 2010:3(4):691–705. https://doi.org/10.1093/mp/ssq025
- Dempsey GT, Vaughan JC, Chen KH, Bates M, Zhuang X. Evaluation of fluorophores for optimal performance in localization-based super-resolution imaging. *Nat Methods*. 2011:8(12):1027–1036. https://doi.org/10.1038/nmeth.1768
- Dignon GL, Zheng W, Kim YC, Mittal J. Temperature-controlled liquid-liquid phase separation of disordered proteins. ACS Cent Sci. 2019:5(5):821–830. https://doi.org/10.1021/acscentsci.9b00102
- Dong X, Qu G, Piazza CL, Belfort M. Group II intron as cold sensor for self-preservation and bacterial conjugation. *Nucleic Acids Res.* 2020:48(11):6198–6209. https://doi.org/10.1093/nar/gkaa313
- Dupouy G, McDermott E, Cashell R, Scian A, McHale M, Ryder P, de Groot J, Lucca N, Brychkova G, McKeown PC, et al. Plastid ribosome protein L5 is essential for post-globular embryo development in Arabidopsis thaliana. Plant Reprod. 2022:35(3):189–204. https://doi.org/10.1007/s00497-022-00440-9
- Emenecker RJ, Holehouse AS, Strader LC. Emerging roles for phase separation in plants. *Dev Cell*. 2020:55(1):69–83. https://doi.org/10.1016/j.devcel.2020.09.010
- Fang X, Wang L, Ishikawa R, Li Y, Fiedler M, Liu F, Calder G, Rowan B, Weigel D, Li P, et al. Arabidopsis FLL2 promotes liquid–liquid phase separation of polyadenylation complexes. *Nature*. 2019:569(7755): 265–269. https://doi.org/10.1038/s41586-019-1165-8
- Farrow NA, Muhandiram R, Singer AU, Pascal SM, Kay CM, Gish G, Shoelson SE, Pawson T, Forman-Kay JD, Kay LE. Backbone dynamics of a free and phosphopeptide-complexed Src homology 2 domain studied by 15N NMR relaxation. *Biochemistry*. 1994:33: 5984–6003. https://doi.org/10.1021/bi00185a040
- Félix SS, Laurents DV, Oroz J, Cabrita EJ. Fused in sarcoma undergoes cold denaturation: implications for phase separation. *Protein Sci.* 2023:32(1):e4521. https://doi.org/10.1002/pro.4521
- Fernández-Suárez M, Ting AY. Fluorescent probes for superresolution imaging in living cells. Nat Rev Mol Cell Biol. 2008:9-(12):929–943. https://doi.org/10.1038/nrm2531
- Field S, Jang G-J, Dean C, Strader LC, Rhee SY. Plants use molecular mechanisms mediated by biomolecular condensates to integrate environmental cues with development. *Plant Cell*. 2023:35(9): 3173–3186. https://doi.org/10.1093/plcell/koad062

- Forman-Kay JD, Mittag T. From sequence and forces to structure, function, and evolution of intrinsically disordered proteins. Structure. 2013:21(9):1492-1499. https://doi.org/10.1016/j.str.2013. 08.001
- François P, Arbes H, Demais S, Baudin-Baillieu A, Namy O. RiboDoc: a docker-based package for ribosome profiling analysis. Comput Struct Biotechnol J. 2021:19:2851-2860. https://doi.org/10.1016/j. csbj.2021.05.014
- Franzmann TM, Alberti S. Prion-like low-complexity sequences: key regulators of protein solubility and phase behavior. J Biol Chem. 2019:294(18):7128-7136. https://doi.org/10.1074/jbc.TM118.001190
- Gao Y, Thiele W, Saleh O, Scossa F, Arabi F, Zhang H, Sampathkumar A, Kühn K, Fernie A, Bock R, et al. Chloroplast translational regulation uncovers nonessential photosynthesis genes as key players in plant cold acclimation. Plant Cell. 2022:34(5):2056-2079. https://doi.org/10.1093/plcell/koac056
- Gueroussov S, Weatheritt RJ, O'Hanlon D, Lin Z-Y, Narula A, Gingras A-C, Blencowe BJ. Regulatory expansion in mammals of multivalent hnRNP assemblies that globally control alternative splicing. Cell. 2017:170(2):324-339.e23. https://doi.org/10.1016/j.cell.2017. 06.037
- Gutierrez-Beltran E, Strader L, Bozhkov PV. Focus on biomolecular condensates. Plant Cell. 2023:35(9):3155-3157. https://doi.org/10. 1093/plcell/koad182
- Hajdukiewicz PT, Allison LA, Maliga P. The two RNA polymerases encoded by the nuclear and the plastid compartments transcribe distinct groups of genes in tobacco plastids. EMBO J. 1997:16(13): 4041-4048. https://doi.org/10.1093/emboj/16.13.4041
- Hanson J, Paliwal K, Litfin T. Enhancing protein intrinsic disorder prediction by utilizing deep squeeze and excitation residual inception and long short-term memory networks. Genom Proteom Bioinf. 2019:17(6):645-656. https://doi.org/10.1016/j.gpb.2019.01.
- Hoffmann G, López-González S, Mahboubi A, Hanson J, Hafrén A. Cauliflower mosaic virus protein P6 is a multivalent node for RNA granule proteins and interferes with stress granule responses during plant infection. Plant Cell. 2023:35(9):3363-3382. https://doi.org/10.1093/plcell/koad101
- Hofmann S, Cherkasova V, Bankhead P, Bukau B, Stoecklin G. Translation suppression promotes stress granule formation and cell survival in response to cold shock. Mol Biol Cell. 2012:23(19): 3786-3800. https://doi.org/10.1091/mbc.e12-04-0296
- Huang S, Zhu S, Kumar P, MacMicking JD. A phase-separated nuclear GBPL circuit controls immunity in plants. Nature. 2021a:594-(7863):424-429. https://doi.org/10.1038/s41586-021-03572-6
- Huang X, Chen S, Li W, Tang L, Zhang Y, Yang N, Zou Y, Zhai X, Xiao N, Liu W, et al. ROS regulated reversible protein phase separation synchronizes plant flowering. Nat Chem Biol. 2021b:17(5):549-557. https://doi.org/10.1038/s41589-021-00739-0
- Ivanov P, Kedersha N, Anderson P. Stress granules and processing bodies in translational control. Cold Spring Harb Perspect Biol. 2019:11(5):a032813. https://doi.org/10.1101/cshperspect.a032813
- Jones PG, Mitta M, Kim Y, Jiang W, Inouye M. Cold shock induces a major ribosomal-associated protein that unwinds doublestranded RNA in Escherichia coli. Proc Natl Acad Sci U S A. 1996:93(1):76-80. https://doi.org/10.1073/pnas.93.1.76
- Jourdain AA, Boehm E, Maundrell K, Martinou J-C. Mitochondrial RNA granules: compartmentalizing mitochondrial gene expression. J Cell Biol. 2016:212(6):611-614. https://doi.org/10.1083/jcb. 201507125
- Jung J-H, Barbosa AD, Hutin S, Kumita JR, Gao M, Derwort D, Silva CS, Lai X, Pierre E, Geng F, et al. A prion-like domain in ELF3 functions

- as a thermosensor in Arabidopsis. Nature. 2020:585(7824): 256-260. https://doi.org/10.1038/s41586-020-2644-7
- Kang H, Xu T. N6-methyladenosine RNA methylation modulates liquid-liquid phase separation in plants. Plant Cell. 2023:35(9): 3205-3213. https://doi.org/10.1093/plcell/koad103
- Kato M, Han TW, Xie S, Shi K, Du X, Wu LC, Mirzaei H, Goldsmith EJ, Longgood J, Pei J, et al. Cell-free formation of RNA granules: low complexity sequence domains form dynamic fibers within hydrogels. Cell. 2012:149(4):753-767. https://doi.org/10.1016/j.cell.2012. 04.017
- Kearly A, Nelson ADL, Skirycz A, Chodasiewicz M. Composition and function of stress granules and P-bodies in plants. Semin Cell Dev Biol. 2022:156:167-175. https://doi.org/10.1016/j.semcdb.2022.11.
- Kim EY, Wang L, Lei Z, Li H, Fan W, Cho J. Ribosome stalling and SGS3 phase separation prime the epigenetic silencing of transposons. Nat Plants. 2021:7(3):303-309. https://doi.org/10.1038/s41477-021-
- Klughammer C, Schreiber U. Complementary PS II quantum yields calculated from simple fluorescence parameters measured by PAM fluorometry and the saturation pulse method. PAM Appl Notes. 2008:1:201-247. https://www.walz.com/files/downloads/ pan/PAN078007.pdf
- Kraus AJ, Brink BG, Siegel TN. Efficient and specific oligo-based depletion of rRNA. Sci Rep. 2019:9(1):12281. https://doi.org/10.1038/ s41598-019-48692-2
- Kroeger TS, Watkins KP, Friso G, van Wijk KJ, Barkan A. A plantspecific RNA-binding domain revealed through analysis of chloroplast group II intron splicing. Proc Natl Acad Sci U S A. 2009:106-(11):4537-4542. https://doi.org/10.1073/pnas.0812503106
- Kupsch C, Ruwe H, Gusewski S, Tillich M, Small I, Schmitz-Linneweber C. Arabidopsis chloroplast RNA binding proteins CP31A and CP29A associate with large transcript pools and confer cold stress tolerance by influencing multiple chloroplast RNA processing steps. Plant Cell. 2012:24(10):4266-4280. https://doi. org/10.1105/tpc.112.103002
- Kusumi K, Sakata C, Nakamura T, Kawasaki S, Yoshimura A, Iba K. A plastid protein NUS1 is essential for build-up of the genetic system for early chloroplast development under cold stress conditions. Plant J. 2011:68(6):1039-1050. https://doi.org/10.1111/j. 1365-313X.2011.04755.x
- Lancaster AK, Nutter-Upham A, Lindquist S, King OD. PLAAC: a web and command-line application to identify proteins with prion-like amino acid composition. Bioinformatics. 2014:30(17):2501-2502. https://doi.org/10.1093/bioinformatics/btu310
- Lauria F, Tebaldi T, Bernabò P, Groen EJN, Gillingwater TH, Viero G. riboWaltz: optimization of ribosome P-site positioning in ribosome profiling data. PLoS Comput Biol. 2018:14(8):e1006169. https://doi.org/10.1371/journal.pcbi.1006169
- Lee, K, Kang, H. Roles of organellar RNA-binding proteins in plant growth, development, and abiotic stress responses. Int J Mol Sci. 2020:21(12):4548. https://doi.org/10.7150/ijms.39074
- Li C, Fang X. Phase separation as a molecular thermosensor. Dev Cell. 2020:55(2):118–119. https://doi.org/10.1016/j.devcel.2020.09.019
- Li W, Hu J, Shi B, Palomba F, Digman MA, Gratton E, Jiang H. Biophysical properties of AKAP95 protein condensates regulate splicing and tumorigenesis. Nat Cell Biol. 2020:22(8):960-972. https://doi.org/10.1038/s41556-020-0550-8
- Li YQ, Sugiura M. Nucleic acid-binding specificities of tobacco chloroplast ribonucleoproteins. Nucleic Acids Res. 1991:19(11): 2893–2896. https://doi.org/10.1093/nar/19.11.2893
- Liebers M, Cozzi C, Uecker F, Chambon L, Blanvillain R, Pfannschmidt T. Biogenic signals from plastids and their role in chloroplast

- development. J Exp Bot. 2022:73(21):7105–7125. https://doi.org/10.1093/jxb/erac344
- Lindquist JA, Mertens PR. Cold shock proteins: from cellular mechanisms to pathophysiology and disease. *Cell Commun Signal*. 2018:16(1):63. https://doi.org/10.1186/s12964-018-0274-6
- Liu X, Rodermel SR, Yu F. A var2 leaf variegation suppressor locus, SUPPRESSOR OF VARIEGATION3, encodes a putative chloroplast translation elongation factor that is important for chloroplast development in the cold. BMC Plant Biol. 2010:10(1):287. https://doi.org/10.1186/1471-2229-10-287
- Majeran W, Friso G, Asakura Y, Qu X, Huang M, Ponnala L, Watkins KP, Barkan A, van Wijk KJ. Nucleoid-enriched proteomes in developing plastids and chloroplasts from maize leaves: a new conceptual framework for nucleoid functions. *Plant Physiol.* 2011:158(1): 156–189. https://doi.org/10.1104/pp.111.188474
- Manalastas-Cantos K, Konarev PV, Hajizadeh NR, Kikhney AG, Petoukhov MV, Molodenskiy DS, Panjkovich A, Mertens HDT, Gruzinov A, Borges C, et al. ATSAS 3.0: expanded functionality and new tools for small-angle scattering data analysis. *J Appl Crystallogr.* 2021:54(1):343–355. https://doi.org/10.1107/S16005767 20013412
- McSwiggen DT, Mir M, Darzacq X, Tjian R. Evaluating phase separation in live cells: diagnosis, caveats, and functional consequences. *Genes Dev.* 2019:33(23–24):1619–1634. https://doi.org/10.1101/gad.331520.119
- Molliex A, Temirov J, Lee J, Coughlin M, Kanagaraj AP, Kim HJ, Mittag T, Taylor JP. Phase separation by low complexity domains promotes stress granule assembly and drives pathological fibrillization. Cell. 2015:163(1):123–133. https://doi.org/10.1016/j.cell.2015. 09.015
- Nakamura T, Ohta M, Sugiura M, Sugita M. Chloroplast ribonucleoproteins are associated with both mRNAs and intron-containing precursor tRNAs. FEBS Lett. 1999:460(3):437–441. https://doi.org/ 10.1016/S0014-5793(99)01390-3
- Nakamura T, Ohta M, Sugiura M, Sugita M. Chloroplast ribonucleoproteins function as a stabilizing factor of ribosome-free mRNAs in the stroma. *J Biol Chem.* 2001:276(1):147–152. https://doi.org/10.1074/jbc.M008817200
- Nott TJ, Petsalaki E, Farber P, Jervis D, Fussner E, Plochowietz A, Craggs TD, Bazett-Jones DP, Pawson T, Forman-Kay JD, et al. Phase transition of a disordered nuage protein generates environmentally responsive membraneless organelles. Mol Cell. 2015:57(5):936–947. https://doi.org/10.1016/j.molcel.2015.01.013
- Ouyang M, Li X, Zhang J, Feng P, Pu H, Kong L, Bai Z, Rong L, Xu X, Chi W, et al. Liquid-liquid phase transition drives intra-chloroplast cargo sorting. *Cell.* 2020:180(6):1144–1159.e20. https://doi.org/10. 1016/j.cell.2020.02.045
- Panchal SC, Bhavesh NS, Hosur RV. Improved 3D triple resonance experiments, HNN and HN(C)N, for HN and 15N sequential correlations in (13C, 15N) labeled proteins: application to unfolded proteins. *J Biomol NMR*. 2001:20(2):135–147. https://doi.org/10.1023/A:1011239023422
- Pearce SF, Rebelo-Guiomar P, D'Souza AR, Powell CA, Van Haute L, Minczuk M. Regulation of mammalian mitochondrial gene expression: recent advances. Trends Biochem Sci. 2017:42(8): 625–639. https://doi.org/10.1016/j.tibs.2017.02.003
- Qamar S, Wang GZ, Randle SJ, Ruggeri FS, Varela JA, Lin JQ, Phillips EC, Miyashita A, Williams D, Ströhl F, et al. FUS phase separation is modulated by a molecular chaperone and methylation of arginine cation-π interactions. *Cell.* 2018:173(3):720–734.e15. https://doi.org/10.1016/j.cell.2018.03.056
- Raab S, Toth Z, de Groot C, Stamminger T, Hoth S. ABA-responsive RNA-binding proteins are involved in chloroplast and stromule

- function in Arabidopsis seedlings. Planta. 2006:224(4):900–914. https://doi.org/10.1007/s00425-006-0282-4
- Rey T, Zaganelli S, Cuillery E, Vartholomaiou E, Croisier M, Martinou J-C, Manley S. Mitochondrial RNA granules are fluid condensates positioned by membrane dynamics. *Nat Cell Biol.* 2020:22(10): 1180–1186. https://doi.org/10.1038/s41556-020-00584-8
- Riback JA, Katanski CD, Kear-Scott JL, Pilipenko EV, Rojek AE, SosnickTR, Drummond DA. Stress-triggered phase separation is an adaptive, evolutionarily tuned response. *Cell.* 2017:168(6): 1028–1040.e19. https://doi.org/10.1016/j.cell.2017.02.027
- Richter AS, Nägele T, Grimm B, Kaufmann K, Schroda M, Leister D, Kleine T. Retrograde signaling in plants: a critical review focusing on the GUN pathway and beyond. *Plant Commun.* 2023:4(1): 100511. https://doi.org/10.1016/j.xplc.2022.100511
- Roden C, Gladfelter AS. RNA contributions to the form and function of biomolecular condensates. *Nat Rev Mol Cell Biol.* 2021:22(3): 183–195. https://doi.org/10.1038/s41580-020-0264-6
- Rosenzweig ESF, Xu B, Cuellar LK, Martinez-Sanchez A, Schaffer M, Strauss M, Cartwright HN, Ronceray P, Plitzko JM, Förster F, et al. The eukaryotic CO₂-concentrating organelle is liquid-like and exhibits dynamic reorganization. *Cell.* 2017:171(1): 148–162.e19. https://doi.org/10.1016/j.cell.2017.08.008
- Roy S, Ueda M, Kadowaki K-I, Tsutsumi N. Different status of the gene for ribosomal protein S16 in the chloroplast genome during evolution of the genus Arabidopsis and closely related species. *Genes Genet Syst.* 2010:85(5):319–326. https://doi.org/10.1266/ggs. 85.319
- Ruiz-Solaní N, Salguero-Linares J, Armengot L, Santos J, Pallarès I, van Midden KP, Phukkan UJ, Koyuncu S, Borràs-Bisa J, Li L, et al. Arabidopsis metacaspase MC1 localizes in stress granules, clears protein aggregates, and delays senescence. *Plant Cell*. 2023:35(9): 3325–3344. https://doi.org/10.1093/plcell/koad172
- Ruwe H, Kupsch C, Teubner M, Schmitz-Linneweber C. The RNA-recognition motif in chloroplasts. J. Plant Physiol. 2011:168-(12):1361–1371. https://doi.org/10.1016/j.jplph.2011.01.012
- Sattler M. Heteronuclear multidimensional NMR experiments for the structure determination of proteins in solution employing pulsed field gradients. *Prog Nucl Magn Reson Spectrosc.* 1999:34(2): 93–158. https://doi.org/10.1016/S0079-6565(98)00025-9
- Schwenkert S, Legen J, Takami T, Shikanai T, Herrmann RG, Meurer J. Role of the low-molecular-weight subunits PetL, PetG, and PetN in assembly, stability, and dimerization of the cytochrome b6f complex in tobacco. *Plant Physiol.* 2007:144(4):1924–1935. https://doi.org/10.1104/pp.107.100131
- Shang B, Wang L, Yan X, Li Y, Li C, Wu C, Wang T, Guo X, Choi SW, Zhang T, et al. Intrinsically disordered proteins SAID1/2 condensate on SERRATE for dual inhibition of miRNA biogenesis in Arabidopsis. Proc Natl Acad Sci U S A. 2023:120(14):e2216006120. https://doi.org/10.1073/pnas.2216006120
- Shen Y, Bax A. Protein backbone and sidechain torsion angles predicted from NMR chemical shifts using artificial neural networks. *J Biomol NMR*. 2013:56(3):227–241. https://doi.org/10.1007/s10858-013-9741-y
- Shin Y, Brangwynne CP. Liquid phase condensation in cell physiology and disease. Science. 2017:357(6357):eaaf4382. https://doi.org/10.1126/science.aaf4382
- Small I, Melonek J, Bohne A-V, Nickelsen J, Schmitz-Linneweber C. Plant organellar RNA maturation. Plant Cell. 2023:35(6): 1727–1751. https://doi.org/10.1093/plcell/koad049
- Solis-Miranda J, Chodasiewicz M, Skirycz A, Fernie AR, Moschou PN, Bozhkov PV, Gutierrez-Beltran E. Stress-related biomolecular condensates in plants. *Plant Cell*. 2023:35(9):3187–3204. https://doi.org/10.1093/plcell/koad127

- Tan H, Luo W, Yan W, Liu J, Aizezi Y, Cui R, Tian R, Ma J, Guo H. Phase separation of SGS3 drives siRNA body formation and promotes endogenous gene silencing. Cell Rep. 2023:42(1):111985. https:// doi.org/10.1016/j.celrep.2022.111985
- Till B, Schmitz-Linneweber C, Williams-Carrier R, Barkan A. CRS1 is a novel group II intron splicing factor that was derived from a domain of ancient origin. RNA. 2001:7(9):1227-1238. https://doi. org/10.1017/S1355838201010445
- Ueda M, Nishikawa T, Fujimoto M, Takanashi H, Arimura S-I, Tsutsumi N, Kadowaki K-I. Substitution of the gene for chloroplast RPS16 was assisted by generation of a dual targeting signal. Mol Biol Evol. 2008:25(8):1566-1575. https://doi.org/10.1093/ molbev/msn102
- Uniacke J, Zerges W. Stress induces the assembly of RNA granules in the chloroplast of Chlamydomonas reinhardtii. J Cell Biol. 2008:182(4):641-646. https://doi.org/10.1083/jcb.200805125
- Uniacke J, Zerges W. Chloroplast protein targeting involves localized translation in Chlamydomonas. Proc Natl Acad Sci U S A. 2009:106(5):1439–1444. https://doi.org/10.1073/pnas.0811268106
- Vranken WF, Boucher W, Stevens TJ, Fogh RH, Pajon A, Llinas M, Ulrich EL, Markley JL, Ionides J, Laue ED. The CCPN data model for NMR spectroscopy: development of a software pipeline. Proteins. 2005:59(4):687–696. https://doi.org/10.1002/prot.20449
- Wang A, Conicella AE, Schmidt HB, Martin EW, Rhoads SN, Reeb AN, Nourse A, Montero DR, Ryan VH, Rohatgi R, et al. A single N-terminal phosphomimic disrupts TDP-43 polymerization, phase separation, and RNA splicing. EMBO J. 2018a:37(5):e97452. https://doi.org/10.15252/embj.201797452
- Wang J, Choi J-M, Holehouse AS, Lee HO, Zhang X, Jahnel M, Maharana S, Lemaitre R, Pozniakovsky A, Drechsel D, et al. A molecular grammar governing the driving forces for phase separation of prion-like RNA binding proteins. Cell. 2018b:174(3): 688-699.e16. https://doi.org/10.1016/j.cell.2018.06.006
- Wang X, Wang J, Li S, Lu C, Sui N. An overview of RNA splicing and functioning of splicing factors in land plant chloroplasts. RNA Biol. 2022:19(1):897-907. https://doi.org/10.1080/15476286.2022.
- Wang W, Wang C, Wang Y, Ma J, Wang T, Tao Z, Liu P, Li S, Hu Y, Gu A, et al. The P-body component DECAPPING5 and the floral repressor SISTER OF FCA regulate FLOWERING LOCUS C transcription in Arabidopsis. Plant Cell. 2023:35(9):3303-3324. https://doi. org/10.1093/plcell/koad151

- Woodruff JB, Gomes BF, Widlund PO, Mahamid J, Honigmann A, Hyman AA. The centrosome is a selective condensate that nucleates microtubules by concentrating tubulin. Cell. 2017:169(6): 1066-1077.e10. https://doi.org/10.1016/j.cell.2017.05.028
- Xie D, Chen M, Niu J, Wang L, Li Y, Fang X, Li P, Qi Y. Phase separation of SERRATE drives dicing body assembly and promotes miRNA processing in Arabidopsis. Nat Cell Biol. 2021;23(1):32-39. https:// doi.org/10.1038/s41556-020-00606-5
- Ye L, Sugiura M. Domains required for nucleic acid binding activities in chloroplast ribonucleoproteins. Nucleic Acids Res. 1992:20(23): 6275-6279. https://doi.org/10.1093/nar/20.23.6275
- Ying Y, Wang X-J, Vuong CK, Lin C-H, Damianov A, Black DL. Splicing activation by Rbfox requires self-aggregation through its tyrosine-rich domain. Cell. 2017:170(2):312-323.e10. https://doi. org/10.1016/j.cell.2017.06.022
- Yoo S-D, Cho Y-H, Sheen J. Arabidopsis mesophyll protoplasts: a versatile cell system for transient gene expression analysis. Nat Protoc. 2007:2(7):1565-1572. https://doi.org/10.1038/nprot.2007.199
- Yoshizawa T, Ali R, Jiou J, Fung HYJ, Burke KA, Kim SJ, Lin Y, Peeples WB, Saltzberg D, Soniat M, et al. Nuclear import receptor inhibits phase separation of FUS through binding to multiple sites. Cell. 2018:173(3):693-705.e22. https://doi.org/10.1016/j.cell.2018.03. 003
- Zavaliev R, Mohan R, Chen T, Dong X. Formation of NPR1 condensates promotes cell survival during the plant immune response. Cell. 2020:182(5):1093-1108.e18. https://doi.org/10.1016/j.cell.2020.07.
- Zhang Y, Fan S, Hua C, Teo ZWN, Kiang JX, Shen L, Yu H. Phase separation of HRLP regulates flowering time in Arabidopsis. Sci Adv. 2022:8(25):eabn5488. https://doi.org/10.1126/sciadv.abn5488
- Zhao C, Pyle AM. Structural insights into the mechanism of group II intron splicing. Trends Biochem Sci. 2017:42(6):470–482. https://doi. org/10.1016/j.tibs.2017.03.007
- Zhu P, Lister C, Dean C. Cold-induced Arabidopsis FRIGIDA nuclear condensates for FLC repression. Nature. 2021:599:657-661. https://doi.org/10.1038/s41586-021-04062-5
- Zoschke R, Bock R. Chloroplast translation: structural and functional organization, operational control, and regulation. Plant Cell. 2018:30(4):745-770. https://doi.org/10.1105/tpc.18.00016
- Zoschke R, Watkins KP, Barkan A. A rapid ribosome profiling method elucidates chloroplast ribosome behavior in vivo. Plant Cell. 2013:25(6):2265-2275. https://doi.org/10.1105/tpc.113.111567